



Role of interfacial oxygen vacancies in low-loaded Au-based catalysts for the low-temperature reverse water gas shift reaction

Abdallah.I. M. Rabee^{a,b,*}, Dan Zhao^a, Sebastian Cisneros^a, Carsten R. Kreyenschulte^a, Vita Kondratenko^a, Stephan Bartling^a, Christoph Kubis^a, Evgenii V. Kondratenko^a, Angelika Brückner^{a,c}, Jabor Rabeah^{a,**}

^a Leibniz-Institut für Katalyse, Albert-Einstein-Str. 29 A, 18059 Rostock, Germany

^b Chemistry Department, Faculty of Science, Minia University, El-Minia 61519, Egypt

^c Department Life, Light and Matter, University of Rostock, Albert-Einstein-Str. 25, 18059 Rostock, Germany

ARTICLE INFO

Keywords:

CO₂ hydrogenation
Reverse water–gas shift
Gold
Operando spectroscopy
Oxygen vacancy

ABSTRACT

Gold-based catalysts have shown high catalytic activity for reverse water gas shift (RWGS) reactions at low temperatures. Despite extensive studies, the RWGS reaction on Au-based catalysts with very low Au content (< 0.1 wt%) has not yet been investigated. In this study, TiO₂ and ZrO₂ supported gold catalysts with such low gold loading have been synthesized and tested for RWGS. The catalysts were investigated by a series of *in/ex-situ* characterization techniques, including ICP-OES, XRD, BET, XPS, STEM, STEM-EELS, TAP, *in-situ* DRIFTS and *in-situ* EPR. At 250 °C, the Au/TiO₂ catalyst showed almost 10 times higher activity than Au/ZrO₂. *In-situ* DRIFTS results suggest that the formate mechanism is the predominant mechanism over Au/ZrO₂, while over Au/TiO₂ the reaction proceeds via the formation of hydroxycarbonyl intermediates. A combined study including STEM, STEM-EELS, XPS, and *in-situ* EPR suggests that the interfacial Au–O_v–Ti³⁺ sites are responsible for the superior activity of Au/TiO₂.

1. Introduction

Fossil fuel emissions, particularly CO₂, are associated with serious environmental issues such as global warming, ocean acidification, and climate change. Hence, rigorous control and reduction of such emissions is absolutely urgent. The reverse water gas shift (RWGS) reaction (CO₂ + H₂ → CO + H₂O ΔH_{298K}⁰ = 41.1 kJ/mol) offers an opportunity to tackle such an issue [1]. As CO is an important chemical feedstock for the synthesis of fine chemicals and fuels via a variety of well-established catalytic approaches (e.g., Fischer–Tropsch (FT) synthesis [2]), the reuse of waste CO₂ gas via RWGS is clearly helpful for mitigating global warming while facing the depletion of fossil fuels. Therefore, the search for stable, active, and selective heterogeneous catalysts to convert CO₂ into CO is a worthwhile task [3].

Many attempts have been made to use transition-metal-based catalysts for the RWGS reaction. Much attention was paid to Cu-containing materials as replacement for expensive noble catalysts based on gold. However, despite their high activity, Cu catalysts cannot surpass the

performance of noble metal-based catalysts, particularly at low reaction temperatures. Transition-metal-based catalysts also exhibit relatively low intrinsic activity and require large metal loadings [4]. Additionally, clusters of such transition metals tend to segregate into large particles, resulting in a loss of activity [4–8].

Au-based catalysts have been extensively studied for CO₂ hydrogenation in the past decades due to their excellent activity under mild reaction conditions [9–13]. Since molecular H₂ activation is an intermediate step in the CO₂ hydrogenation reaction [14,15], the size of supported gold species governs their catalytic activity. Bulk gold is known to be inactive for H₂ dissociation due to weak interaction with molecular H₂ [13], however, this step is markedly promoted by supported metal nanoparticles (NPs) and clusters [11,16–18]. In addition, several studies have shown that the activity of Au-based catalysts in CO₂ hydrogenation reactions depends strongly on the type of the support [19], since activation of CO₂ mainly occurs at the oxide support or the interfacial sites between metal and support [20]. Moreover, the catalytic activity of Au-based catalyst can be modified by tuning metal–support

* Corresponding author at: Leibniz-Institut für Katalyse, Albert-Einstein-Str. 29 A, 18059 Rostock, Germany.

** Corresponding author.

E-mail addresses: Abdallah.Ahmed@catalysis.de (Abdallah.I.M. Rabee), Jabor.Rabeah@catalysis.de (J. Rabeah).

interactions (i.e., the electron transfer between Au and support). Au supported on different metal oxides such as TiO_2 [11,13,21], ZrO_2 [11], Fe_2O_3 [11], CeO_2 [11,12], and Al_2O_3 [13], has been reported to be active for low temperature RWGS reaction. Sakurai et al. [11] also reported that acid-base properties of supports play a decisive role for RWGS activity. They studied CO_2 hydrogenation on a variety of supported Au catalysts with different carriers (TiO_2 , Fe_2O_3 , ZrO_2 , CeO_2 , ZnO , $\text{La}(\text{OH})_3$) and found a direct correlation between CO_2 conversion and surface acidity, whereby TiO_2 , Fe_2O_3 and ZrO_2 revealed to be most promising [11]. They found higher activities for Au NPs supported on acidic supports than on basic supports which was traced back to differences in the interaction of CO_2 with the support [11]. The relatively weak adsorption of CO_2 on acidic supports led to a higher CO_2 hydrogenation activity [11].

Furthermore, it has been reported that prereduced TiO_2 is more active for reduction of CO_2 , due to higher density of point defects (oxygen vacancies and Ti^{3+}) formed during pre-treatment in hydrogen. Oxygen vacancies and Ti^{3+} on the TiO_2 surface significantly improve adsorption of CO_2 [13,22] and enhance metal-support interactions [23, 24]. ZrO_2 is also a promising support material for many catalytic reactions, due to its high thermal stability, amphoteric, and redox properties [25,26]. The presence of defects such as oxygen vacancies and Zr^{3+} is also reported in ZrO_2 [26]. However, the impact of oxygen vacancies in ZrO_2 on the reaction mechanism of RWGS is less investigated so far. Fe_2O_3 shows a dynamic phase change under reaction conditions due to a combination of reduction and carburization processes. These phases changes make the study of its catalytic behavior more complicated [27]. Therefore, TiO_2 and ZrO_2 are chosen as catalyst supports in this study.

In all studies mentioned above, high Au loadings ranging from ~1–8 wt% have been used. However, the growing demand for CO_2 hydrogenation requires catalysts with a much lower amount of noble metals due to their high cost and scarcity. To the best of our knowledge, Au catalysts with metal loadings well below 0.1 wt% have not been reported for the RWGS reaction so far. Against this background, our aim was to develop Au/ TiO_2 and Au/ ZrO_2 catalysts with Au loadings as low as 0.1 wt% and to provide new insights into the role of the oxygen vacancies for CO_2 hydrogenation to CO. The effects of reaction temperature, pressure, and gas hourly space velocity (GHSV) on CO_2 conversion and CO selectivity were investigated. Catalyst characterization by the Brunauer-Emmett-Teller (BET) method, X-ray Powder Diffraction (XRD), X-ray photoelectron spectroscopy (XPS), scanning transmission electron microscopy (STEM) and electron energy loss spectroscopy (EELS) was performed to establish structure-performance relationships. Temporal analysis of products (TAP) was used to study the interaction of CO_2 and CO with the catalysts. In addition, in-situ diffuse reflectance, infrared Fourier transform spectroscopy (DRIFTS), and in-situ electron paramagnetic resonance (EPR) were employed to investigate the key reaction intermediate and the role of oxygen vacancies under real reaction conditions.

2. Experimental section

2.1. Material and catalyst preparation

Aeroxide TiO_2 P25 was provided by Evonik Industries and used as received. Pure ZrO_2 was synthesized by precipitation in aqueous solution at 25 °C. 1 M NaOH (99.1%, Fisher Chemical) was added dropwise to 200 ml of 0.1 M $\text{ZrOCl}_2 \cdot 0.8 \text{H}_2\text{O}$ (98%, Alfa Aesar) under stirring. The precipitate was left for 1 h in contact with the mother liquor and then filtered, washed with distilled water, and dried at 100 °C for 12 h. The dried material was ground and calcined at 500 °C (at 2 °C/min) for 3 h under synthetic air flow.

Au/ TiO_2 and Au/ ZrO_2 catalysts with a nominal Au loading of 0.1 wt % were prepared by a deposition–precipitation method. Typically, 1.0 g of the support powder was added to 20 ml of an aqueous solution of

HAuCl_4 (99.995%, Sigma-Aldrich). The pH of the solutions was then adjusted to ~9 by adding 0.1 M NaOH dropwise. The suspensions were stirred at 25 °C for 2 h, filtered and washed thoroughly with deionized water. Finally, the samples were dried at 80 °C for 12 h, and then used without any further heat treatment.

2.2. Catalyst characterization

Before the characterization, the catalysts were reduced at 300 °C in 50% H_2/N_2 for 2 h with a total flow rate of 13 ml min^{-1} . The Au content was determined by inductively coupled plasma optical emission spectroscopy (ICP-OES) using a 715-ES ICP emissions spectrometer (Varian, Palo Alto, CA, USA) after subjecting the samples to a microwave-assisted digestion process in a mixture of HF and aqua regia at 200 °C and 60 bar.

Surface area measurements were performed on a Micromeritics ASAP 2010 device. The average pore diameters were calculated from the desorption branch of the isotherm using the BJH method. Prior to N_2 adsorption, 150 mg of the reduced catalysts were placed in the analysis tube and outgassed at 200 °C for 4 h.

XRD patterns were recorded using a PANalytical X'Pert PRO diffractometer equipped with a X'Celerator RTMS detector using Ni-filtered $\text{Cu-K}\alpha$ radiation (1.54443 Å) at 40 kV and 40 mA. Samples were mounted on silicon zero background holders, and the data were acquired stepwise (0.021°/s) between 5 and 100° with a divergence slit of 2°. Peak positions and profiles were fitted with a Pseudo-Voigt function using the HighScore Plus software package (Panalytical). Phase identification was done using the PDF-2 database of the International Center of Diffraction Data (ICDD).

X-ray Photoelectron Spectra (XPS) were recorded on an ESCALAB 220iXL (Thermo Fisher Scientific) with monochromated Al $\text{K}\alpha$ radiation ($E = 1486.6 \text{ eV}$). The catalysts were deposited on a stainless-steel holder with conductive double-sided adhesive carbon tape. The electron binding energies were obtained with charge compensation using a flood electron source and referenced to the C 1s core level of carbon at 284.8 eV (C-C and C-H bonds). For quantitative analysis, the peaks were deconvoluted with Gaussian-Lorentzian curves using Unifit 2021. The peak areas were normalized by the transmission function of the spectrometer and the element-specific sensitivity factor of Scofield [28].

Scanning transmission electron microscopy (STEM) measurements were performed with an aberration-corrected JEM-ARM200F (Jeol, Corrector: CEOS) at 200 kV. It is equipped with a Gatan Enfium ER electron energy loss spectrometer (EELS). A High-Angle Annular Dark Field (HAADF) and an Annular Bright Field (ABF) detector were used for STEM imaging, while during EELS acquisition, the Annular Dark Field (ADF) detector was used to acquire the positional reference image. The catalysts were deposited without further treatment onto a copper grid with holey carbon support (mesh 300), which was then transferred to the microscope.

2.3. In-situ DRIFTS measurements

In-situ DRIFT spectra were obtained using a Nicolet iS10 (Thermo Fischer Scientific) FTIR spectrometer using a high-temperature Praying Mantis reaction cell (Harrick) with CaF_2 windows equipped with a temperature control unit (Eurotherm) and connected to a gas dosing system with mass-flow controllers (Bronkhorst). The spectra were recorded (averaged 64 scans) in the frequency range of 4000–400 cm^{-1} at a resolution of 4 cm^{-1} . Ca. 25 mg of pure catalyst powder was deposited on top of a layer of 80 mg pure $\alpha\text{-Al}_2\text{O}_3$ (pre-calcined at 900 °C in synthetic air for 8 h) within the sample cup. Before the reaction, a reductive pretreatment in a stream of 50% H_2/He (13 ml min^{-1}) was performed for 2 h at 300 °C. Subsequently, the reaction cell was purged with He at 18 ml min^{-1} for 30 min to evacuate the H_2 . Afterward, the temperature was reduced to 250 °C, and the cell pressure was increased to 3 bar under He flow at this temperature. Once the desired pressure was reached the gas was switched to the reaction mixture with

a H₂: CO₂ ratio of 3:1 (9.0 ml min⁻¹ H₂, 3.0 ml min⁻¹ CO₂, 6.0 ml min⁻¹ He, 2.0 ml min⁻¹ Ne). The Neon (Ne) is used as internal calibration gas for the quadrupole mass spectrometer (Omnistar, Pfeiffer Vacuum gmbh) which is connected to the gas outlet for online product analysis. After 90 min reaction at 250 °C, the temperature was increased to 300 °C and finally to 350 °C. For each step, the reaction was followed for 90 min. The intensity of the signals is given on the log(1/R) scale.

2.4. In-situ EPR measurements

In-situ EPR spectra were recorded with a Bruker ELEXSYS 500–10/12 spectrometer operated at X-band frequency at a microwave frequency of 9.32 GHz, a microwave power of 10 mW, and a modulation frequency of 100 kHz. Typically, 65 mg catalyst was placed inside a quartz plug-flow reactor connected to a gas dosing unit equipped with mass flow controllers (Bronkhorst) at the inlet and a quadrupole mass spectrometer (Omnistar, Pfeiffer Vacuum GmbH) at the outlet for online product analysis. Effective *g* values were calculated by Eq. (1).

$$g = \frac{h\nu}{\beta B_0} \quad (1)$$

In which *h* is the Planck constant, *ν* is the microwave frequency, *β* is the Bohr magneton, and *B*₀ is the external magnetic field.

Spectra of fresh catalysts were first recorded at ca. – 173 °C under a flow of 13 ml min⁻¹ He. Afterwards, the gas mixture was switched to 50% H₂/He (13 ml min⁻¹) while the temperature was increased to 280 °C. Under these conditions, the catalyst was reduced for 2 h. Subsequently, the temperature was decreased again to ca. – 173 °C, and the corresponding spectra of the reduced sample were recorded. Next, the temperature was increased to 250 °C in a flow of 13 ml min⁻¹ He. Once the desired temperature was reached, the gas was set to the reaction mixture (9.0 ml min⁻¹ H₂, 3.0 ml min⁻¹ CO₂, 6.0 ml min⁻¹ He, 2.0 ml min⁻¹ Ne). At these conditions, spectra were recorded for 2 h. After the reaction, the temperature was cooled down to ca. – 173 °C, and the corresponding spectra of the spent sample were recorded.

2.5. Temporary Analysis of Products (TAP) experiments

Transient tests were performed in a temporal analysis of products (TAP-2) reactor described in detail elsewhere [29–31]. Typically, 41 mg of a 310–750 μm sieve fraction of each catalytic material was packed between two layers of quartz particles (sieve fraction of 250–355 μm) in a quartz microreactor. Before the transient tests, catalytic materials were heated in an H₂ (3 ml min⁻¹) and Ar (3 ml min⁻¹) flow from room temperature to 300 °C and kept under these conditions for 30 min. Then, the reactor was evacuated to about 10⁻⁵ Pa. Hereafter, mixtures of CO:Ar = 1:1 or CO₂:Ar = 1:1 were pulsed at the same temperature. The feed mixtures were prepared using CO (Messer Griesheim, 4.7), CO₂ (Air Liquide, 4.5), and Ar (Air Liquide, 5.0) without additional purification. Transient responses related to the feed components and reaction products were monitored at the reactor outlet with a quadrupole mass spectrometer (HAL RD 301 Hiden Analytical) at *m/z* signals related to reactants, reaction products, and argon, with the latter being an inert standard: 44 (CO₂), 32 (O₂), 28 (CO₂, CO) and 40 (Ar). For each *m/z*, pulses were repeated 10 times and averaged to improve the signal-to-noise ratio.

Using a model-free approach developed for this technique [30], the experimental responses of CO₂, CO and Ar were transformed into the dimensionless form according to Eqs. (2) and (3). Such transformation allows unambiguously determining the type of interaction of pulsed reactant with catalyst (diffusion, reversible or irreversible adsorption).

$$\text{Dimensionless flow} = \frac{\text{Flux}(\text{CO}_x) \cdot \text{reactor length}^2}{\text{pulse size} \cdot D_{\text{Knudsen}}^{\text{eff}}(\text{CO}_x)} \quad (2)$$

$$\text{Dimensionless time} = \frac{t^* D(\text{CO}_x)}{\text{reactor length}^2} \quad (3)$$

$$\text{Flux}(\text{CO}_x) = I(\text{CO}_x) \frac{N(\text{CO}_x)}{\int_0^t I(\text{CO}_x)} \quad (4)$$

Where *I*(CO_x), *N*(CO_x), and *D*_{Knudsen}^{eff}(CO_x) are the experimental mass spectroscopic signal intensity, the size of pulse, and the diffusion coefficient of CO or CO₂, respectively. To determine the diffusion coefficients of CO and CO₂, the diffusion coefficient of Ar was initially derived by fitting the experimental response to the Knudsen diffusion model as described in Refs. [32,33]. Eq. (5) was used to obtain the required coefficients.

$$D_{\text{Knudsen}}^{\text{eff}}(\text{CO}_x) = D_{\text{Knudsen}}^{\text{eff}}(\text{Ar}) \sqrt{\frac{M(\text{Ar})}{M(\text{CO}_x)}} \quad (5)$$

where *M*(Ar) and *M*(CO_x) are the molecular weights of Ar and CO_x, respectively.

2.6. Catalytic activity measurements

Catalytic tests were carried out using an in-house setup containing 51 continuous-flow fixed-bed stainless-steel tubular reactors operating in parallel. The measurements were conducted in the temperature range of 250–350 °C at a total pressure of 3 and 20 bar. The catalysts were pressed, crushed, and sieved to 310–750 μm. Typically, the reactor (i. d. 4 mm) was filled with 200 mg of catalyst diluted with 800 mg SiC. Reduction of catalysts was performed at 300 °C in 50 vol% H₂/N₂ with a flow rate of 13 ml min⁻¹. After cooling to reaction temperature, a CO₂/H₂/N₂ = 1/3/2 mixture was fed equally to the reactors with two different flow rates (7.25 ml min⁻¹ and 17.5 ml min⁻¹). The reaction products and the feed components were detected with an on-line Agilent HP 7890 gas chromatograph equipped with both FID (FFAP and AL/M columns) and TCD (HP-Plot Q and Molsieve 5 A columns). The conversion of CO₂ was calculated from the inlet and outlet mole flow, as shown in Eq. (6). The selectivity to CO, CH₄ and CH₃OH was calculated using Eq. (7). The rate of CO formation (*r*_{CO}) was calculated by Eq. (8).

$$X_{\text{CO}_2} = \frac{F_{\text{CO}_2, \text{ in}} - F_{\text{CO}_2, \text{ out}}}{F_{\text{CO}_2, \text{ in}}} \times 100\% \quad (6)$$

$$S_x = \frac{F_{x, \text{ in}}}{F_{\text{CO}_2, \text{ in}} - F_{\text{CO}_2, \text{ out}}} \times 100\% \quad (7)$$

$$r_{\text{CO}} = \frac{X_{\text{CO}_2} \times S_{\text{CO}} \times F_{\text{CO}_2}}{10000 \times m_{\text{Au}}} \quad (8)$$

where *X*_{CO₂} is the CO₂ conversion (%), *S*_x is the selectivity to *x* product (%), where *x* is CO, CH₄, or CH₃OH, and *F* is a molar flow rate of CO₂ or product (*x*), *m* is the total amount of Au in gram of catalyst.

3. Results and discussion

3.1. Catalyst characterization

As shown in Table 1, the Au contents in samples Au/TiO₂ and Au/

Table 1
Structural Properties of pure supports and supported gold catalysts.

Catalyst	Au content / %	<i>S</i> _{BET} / m ² g ⁻¹	<i>V</i> _p / cm ³ g ⁻¹	<i>D</i> _p / nm
TiO ₂	–	61.7	0.419	21
Au/TiO ₂	0.05	65.7	0.404	19
ZrO ₂	–	78.5	0.117	4.2
Au/ZrO ₂	0.08	80.6	0.119	4.3

ZrO₂ are 0.05 and 0.08 wt%, respectively. The XRD pattern of TiO₂, ZrO₂, and the corresponding Au-loaded catalysts are shown in Fig. S1. The crystal structure of TiO₂ is a mixture of anatase and rutile, as depicted in Fig. S1a. The reflections at 2θ of 25.5, 37.5, 47.8, 53.8, and 54.9° are assigned to the anatase structure, and the reflections at 2θ of 27.5° and 36.4° are characteristic of the rutile structure [34]. Both bare TiO₂ and Au/TiO₂ samples exhibit the same diffraction pattern without any detectable changes. Identical XRD patterns were also observed for ZrO₂ and Au/ZrO₂ (Fig. S1b), showing the presence of a mixed phase of tetragonal (2θ of 30.15, 34.6, 35.34, 50.61, and 60.17°) and monoclinic (2θ of 24.2, 28.2, 31.5, 34.2, 38.5, 40.7, 50.1, and 54.1°) [35]. No reflections related to Au particles were observed in the patterns of both catalysts, as expected for such low Au contents.

N₂ adsorption-desorption isotherms are shown in Fig. 1. The specific surface area ($S_{\text{BET}}/\text{m}^2\text{g}^{-1}$), total pore volume ($V_p/\text{cm}^3\text{g}^{-1}$), and average pore size values derived therefrom are listed in Table 1. TiO₂ and Au/TiO₂ exhibit Type II isotherms, which are typically obtained with nonporous or macroporous materials [36,37]. Presuming that the detectable pores in powder samples are often inter-particle voids, rather than being structurally defined, we can attribute the observed hysteresis in Fig. 1a to the N₂ condensation in interparticle voids. Fig. 1b shows that ZrO₂ and Au/ZrO₂ exhibit type - IV isotherms with hysteresis loops, indicating the mesoporous nature of the catalysts [37]. The formation of hysteresis at a low relative pressure range ($P/P_0 = 0.45\text{--}0.8$) may be attributed to N₂ condensation in mesopores, which most likely originated from the intraparticle voids. Moreover, from the N₂ adsorption-desorption isotherms in Fig. 1 and the pore characteristics in Table 1, it can be clearly seen that the addition of Au on both supports increased slightly the surface areas, while their average pore sizes were more or less the same, which indicates a high dispersion of the Au species consistent with the XRD results. The slight increase in the surface area of supported Au catalysts compared with the bare supports could be due to the increase in the surface roughness after addition of Au species.

HAADF-STEM was used to probe the existence of gold nanoparticles, clusters, and single-sites over Au/TiO₂ and Au/ZrO₂. Fig. 2a-c presents the representative STEM images of the Au/TiO₂ catalyst. Au species exists almost exclusively as small nanoparticles with an average particle size of 2–3 nm (for more images, see Fig. S2, Supporting Information). Due to the low particle density, it was not feasible to acquire sufficient data for statistical analysis. Fig. 2d-f shows the representative HAADF STEM images of the Au/ZrO₂ catalyst. HAADF imaging is sensitive to atomic number, with heavy atoms appearing as bright dots. According to the high-magnification image (Fig. 2e, f), many of such bright dots are well dispersed on the surface of zirconia, indicating that the vast

majority of Au species is distributed as single sites. For clarity, some Au atoms are indicated by cyan arrows (Fig. 2e, f). A minor fraction of Au species is also found as Au NPs and clusters (Fig. S3).

Because TiO₂ is more reducible than ZrO₂, and the energy loss levels for Zr are not suitable for such an analysis, EELS measurements were only performed to investigate the electronic structure of the Au/TiO₂ catalyst. EEL spectra over the particles' central and interface/surface regions are collected, as marked in Fig. 3. The EELS spectra show a difference in the fine structure of the Ti L_{2,3}-edge, as shown in Fig. 3c, which reveals the presence of two distinct Ti species. The EELS spectrum of the bulk region (red) shows the typical split of the L_{2,3} peaks similar to the Ti L_{2,3}-edge fingerprint of the rutile structure in which Ti species exists as Ti⁴⁺ [38,39]. In contrast, the EEL spectrum (cyan) at the interface region shows two peaks that are not splitted, indicating the potential presence of Ti³⁺ species [38]. EELS oxidation state maps have been calculated from the spectrum imaging dataset by multiple linear least square fits of model spectra from reference areas (like those marked in the STEM-ADF reference image of the spectrum imaging area in Fig. 3a) to confirm further the spatial distributions of the oxidation states of Ti over the particles. Fig. 3b shows the Ti oxidation state map calculated by fitting the reference spectra in Fig. 3c pixelwise to the spectrum imaging dataset. It can be clearly seen that the interface and edge regions of the particles are dominated by Ti³⁺, and the contrast gradient indicates a shell-like distribution.

To get a closer insight into the nature of gold species, the Au 4f XP spectra of the catalysts are recorded and compared in Fig. 4. It is known that the Au 4f_{7/2} binding energy (BE) of metallic Au⁰ is around 84 eV [40]. The binding energies of Au 4f_{7/2} in the XP spectra of Au/TiO₂ and Au/ZrO₂ were found to be 83.4 and 83.9 eV, respectively. These values are close to the BE of Au⁰, thus indicating the metallic character of the supported Au species. Furthermore, a shift of about 0.5 eV to lower binding energies was observed for Au/TiO₂ with respect to Au/ZrO₂. The observed shift in the value of Au 4f_{7/2} BE of Au/TiO₂ catalyst might be correlated with a charge transfer from the oxygen vacancies of the TiO₂ support to Au, leading to a partially negatively charged Au species (Au^{δ-}) compared to the ZrO₂ support.

3.2. Catalytic activity

The catalytic performance for the RWGS reaction of the pure supports and supported Au catalysts was evaluated in the temperature range of 250–350 °C (Fig. 5). After reductive pretreatment with H₂ at 300 °C, the reaction was investigated at 3 bar in a fixed-bed continuous-flow reactor using a feed with the CO₂: H₂: N₂ ratio of 1:3:2 and a total flow

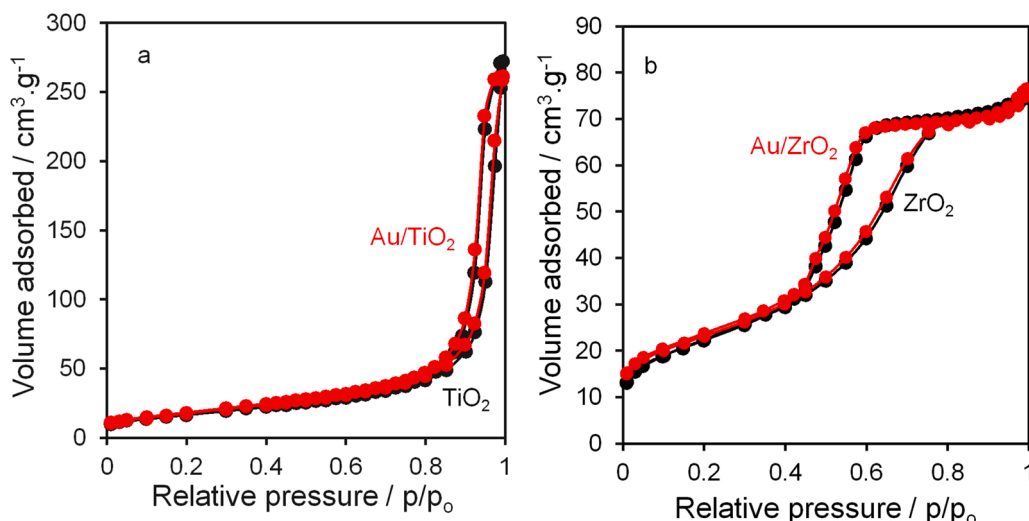


Fig. 1. N₂ adsorption-desorption isotherms at 77 K for (a) pure TiO₂ (black) and Au/TiO₂ catalyst (red) and (b) pure ZrO₂ (black) and Au/ZrO₂ catalyst (red).

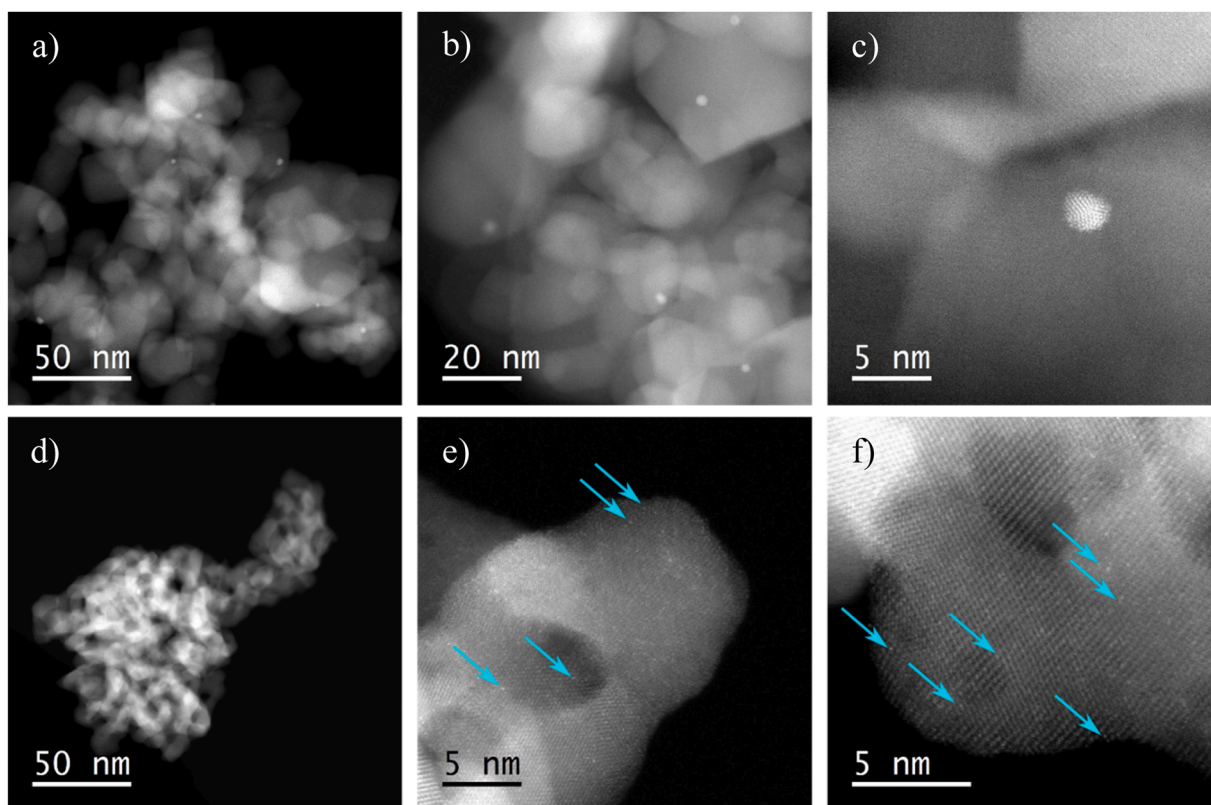


Fig. 2. HAADF STEM images of the (a-c) Au/TiO₂ and (d-f) Au/ZrO₂ catalysts.

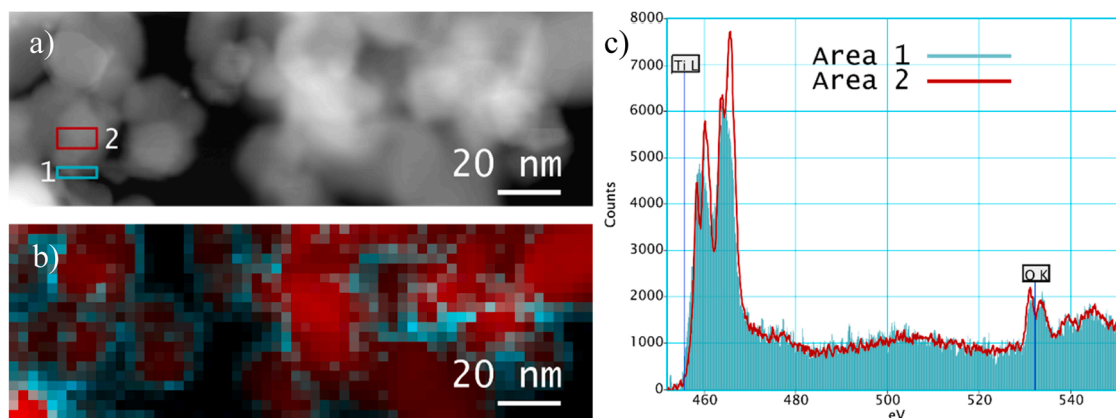


Fig. 3. (a) STEM-ADF image of the Au/TiO₂ catalyst depicting the area used for spectral imaging, (b) the corresponding EELS phase maps of Ti⁴⁺ (red) and the unknown surface species (cyan), and (c) EELS spectra obtained in the two positions marked in (a) with the corresponding color.

rate of 17.5 ml min⁻¹. The CO₂ conversion over both pure supports was low, whereas much higher activities were obtained over the supported Au catalysts under the same reaction conditions (Fig. 5). At 250 °C, Au/TiO₂ afforded a CO₂ conversion of 4.6% with 100% selectivity to CO. In contrast, Au/ZrO₂ shows a poor CO₂ conversion of only 0.8. Over both catalysts, the conversion increased monotonically as the reaction temperature increased from 250° to 350 °C (Fig. 5b).

The rate of CO formation over the Au/TiO₂ catalyst at 250 °C is 69 mmol.g_{Au}⁻¹.min⁻¹, which is almost 10 times higher than that over Au/ZrO₂ catalyst (6.8 mmol.g_{Au}⁻¹.min⁻¹) (Fig. 6a). The activity of Au/TiO₂ rises to ~ 216 mmol.g_{Au}⁻¹.min⁻¹ when the temperature increases to 350 °C. Considering the very low Au loading, the intrinsic activity of our Au/TiO₂ is much higher than other Au-based catalysts that have been reported in the literature (Table S1). The apparent activation energy (*E_a*)

of the RWGS reaction over both catalysts, as shown in Fig. 6b, was determined from the CO formation rate determined between 250 and 350 °C using the classical Arrhenius dependence (Fig. 6b). The *E_a* value over Au/TiO₂ is 31 kJ/mol, in excellent agreement with the previously reported value of 31 kJ/mol over 1 wt% Au/TiO₂ [13] and much lower than that over Au/ZrO₂ (53 kJ/mol). This discrepancy between Au/TiO₂ and Au/ZrO₂ is consistent with the difference in the catalytic activity discussed above. It may suggest a change in the reaction pathways and thereby different rate-determining steps. Several studies attributed the enhancement of the catalytic activity over reducible oxides supported catalysts (e.g., TiO₂) to the direct participation of the support in the reaction mechanism [13,41,42]. The CO formation rates, and *E_a* values are also calculated at 20 bars (Fig. S4). Over both catalysts, the CO formation rates (Fig. S4a) follows the same trend as observed at 3 bar

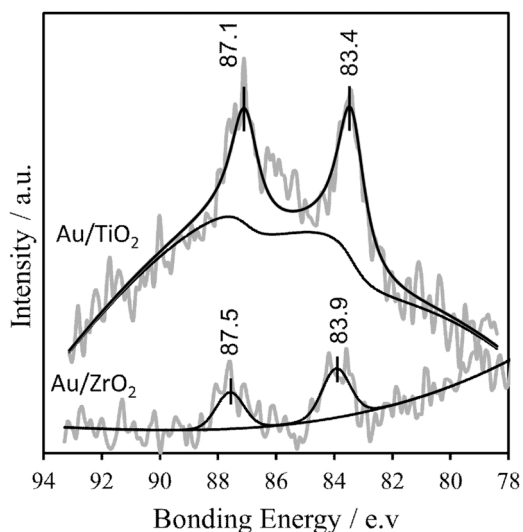


Fig. 4. Au 4f XP spectra of Au/TiO₂ and Au/ZrO₂.

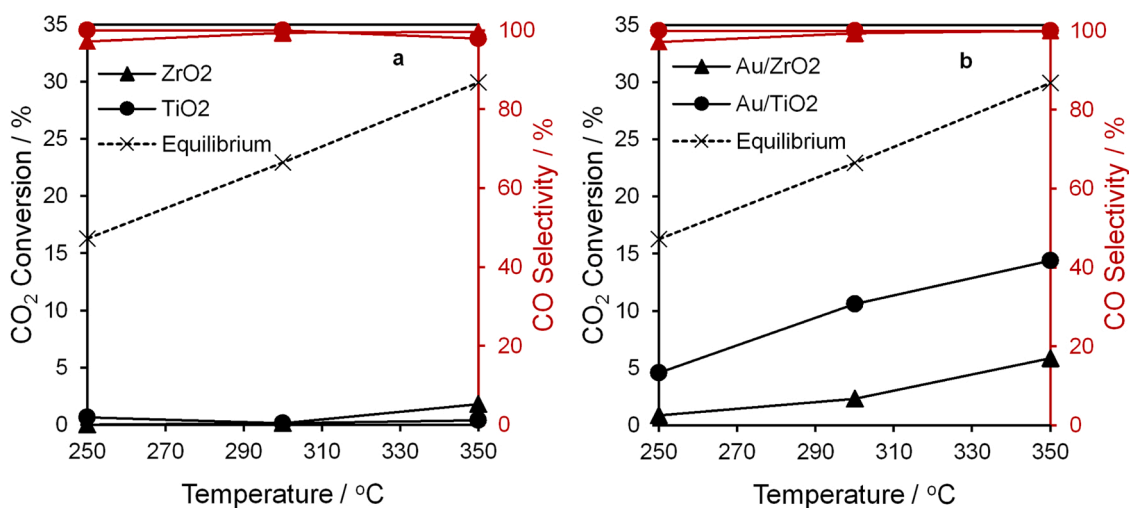


Fig. 5. CO₂ conversion (black) and CO selectivity (red) in % as a function of the testing temperature for (a) pure supports and (b) supported Au catalysts. Reaction condition: $P_{\text{total}} = 3$ bar, CO₂: H₂: N₂ = 1:3:2, GHSV = 5225 ml.g⁻¹.h⁻¹.

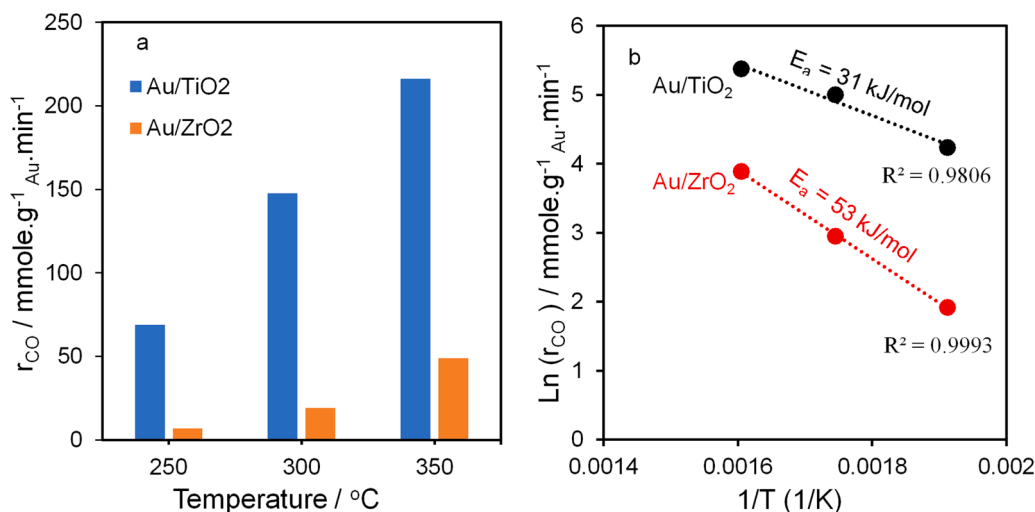


Fig. 6. (a) The rate of CO formation and (b) Arrhenius plots of the rate of CO formation in the temperature range 250–350 °C, over Au/TiO₂ and Au/ZrO₂. Reaction condition: $P_{\text{total}} = 3$ bar, CO₂: H₂: N₂ = 1:3:2, GHSV = 5225 ml.g⁻¹.h⁻¹.

(Fig. 6a). While, interestingly, the E_a values (Fig. 6b and S4b) are almost identical over Au/TiO₂, suggesting a similar reaction mechanism. Whereas, over Au/ZrO₂, the E_a value increased from 53 kJ/mol at 3 bar to 79 kJ/mol at 20 bars. Our results indicate that CO formation rate at 250 °C significantly affect the slope value used to calculate E_a at 20 bars. Compared to the reaction at 3 bar, the increase in the activation barrier for RWGS at 20 bars reduce CO selectivity by 6% (Fig. S6) and raises methane/methanol selectivity by 6% at 250 °C. Moreover, it is also possible that increasing the total pressure results in significant changes in surface coverage of the active intermediate species which in turn might lead to a change in the reaction mechanism and thereby the rate-determining step.

To check if high CO selectivity can be assured at elevated pressures, catalytic tests were carried out at 20 bar using two different values of GHSV (2117 and 5225 ml.g⁻¹.h⁻¹). The results are compared with those obtained at 3 bar in Fig. S5. From a thermodynamic point of view, altering pressure should not affect the equilibrium conversion of the RWGS reaction because there is no variation in the number of moles between the reactants and products while decreasing GHSV should raise the CO₂ conversion due to higher contact time of reactants on the surface of the catalyst. Accordingly, in both catalysts, an increase in CO₂

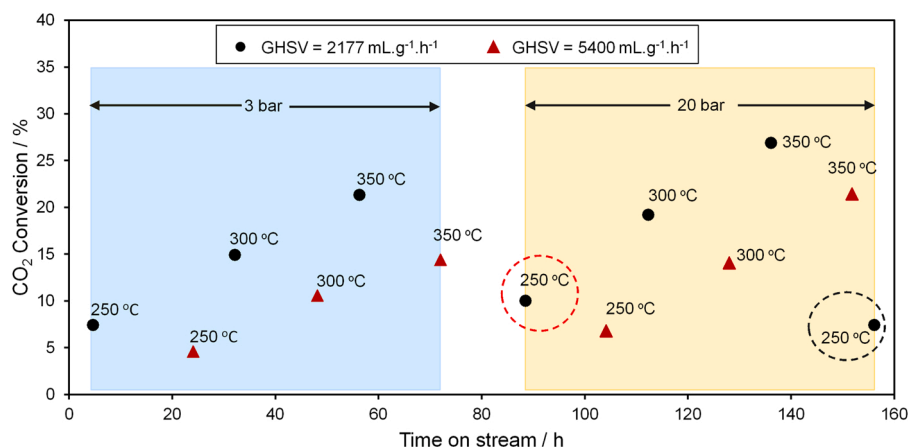


Fig. 7. CO₂ conversion in % as a function of reaction time over Au/TiO₂. Reaction condition: P (bar), T (°C), and GHSV (mL.g⁻¹.h⁻¹) = as indicated, CO₂: H₂: N₂ = 1:3:2.

conversion was observed as the GHSV decreased. In the case of Au/ZrO₂, and at GHSV = 5225 mL.g⁻¹.h⁻¹, significant change was observed when the pressure increased from 3 bar to 20 bar at 300 and 350 °C. The CO₂ conversion was almost twice the conversion obtained at 3 bar, while no appreciable change in CO₂ conversion was noticed at the low temperature of 250 °C. Meanwhile, no noticeable changes in CO selectivity occur. The pressure effect became slightly less significant when the GHSV decreased to 2117 mL.g⁻¹.h⁻¹. On the other hand, for Au/TiO₂ catalyst, the impact of increasing pressure on catalytic performance is less pronounced. It is noteworthy that the CO₂ conversions used in the calculation of CO formation rates over Au/ZrO₂ were well below 10%, thus under almost differential reaction conditions. In addition, by considering the average pore size of Au/ZrO₂ catalyst as well as the molecular dimensions of reactant gases (H₂ and CO₂), we can exclude the possibility of diffusional limitations for the reactants molecules to access the active sites. Therefore, the enhanced activity of Au/ZrO₂ at 20 bars could be explained by the increased coverage of carbon-containing intermediates.

Another point worth noting is the high selectivity to CO under all conditions. Despite the fact that RWGS has a stoichiometric H₂/CO₂ molar ratio of 1:1 [12], the catalytic tests were performed at high H₂/CO₂ ratios of 3. The aim was to verify the catalyst's ability to selectively activate RWGS at hydrogen-rich atmosphere. It is well known that high operating pressure and H₂/CO₂ ratios facilitate further

hydrogenation of CO to methane or methanol; thus, the high CO selectivity under these conditions becomes a challenge [43]. Fig. S6 compares the obtained CO selectivity over both catalysts as a function of reaction temperatures at 3 and 20 bar. A higher selectivity to gaseous CO product was obtained at H₂/CO₂ = 3 over both catalysts, and slight changes in the CO selectivity were observed when the pressure increased from 3 to 20 bar. These results indicate that the catalysts favor the RWGS reaction rather than methanol and methane routes. The superior CO selectivity over both catalysts can be explained by the weak adsorption of the formed CO on Au sites and supports, as proven by the TAP experiments (vide infra, Fig. 9).

To study the ability of the catalyst to recover its catalytic performance, the high-performing catalyst Au/TiO₂ was subjected to a long-term stability test for 158 h (Fig. 7). the CO₂ conversion is compared under identical reaction conditions after two different times on stream. For instance, as shown in Fig. 7, the CO₂ conversion after 82 h (red dotted circle) was compared with the one obtained after 158 h (black dotted circle). It is evident from the results that the catalyst maintains more than 70% of its activity at 82 h, while the CO selectivity remained more than 99% throughout this study. To reveal the causes of the observed catalyst deactivation, HAADF and EELS measurements were performed for the spent Au/TiO₂ catalyst after 158 h (Fig. S7). No notable changes in the Au particle size were visible. EELS-based elemental mapping reveals the presence of carbon at the interface/

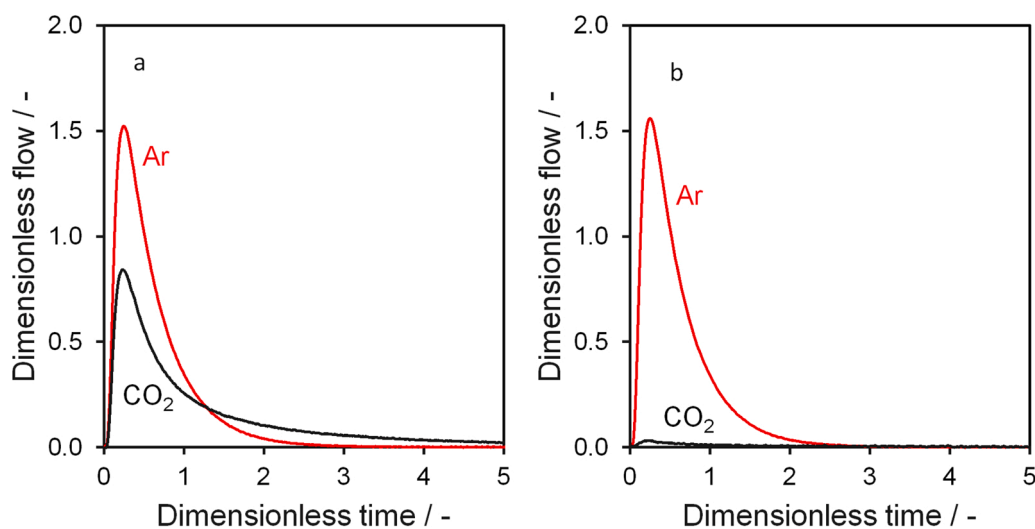


Fig. 8. Single-pulse responses of CO₂ compared with the Ar response at 573 K over (a) Au/TiO₂, and (b) Au/ZrO₂.

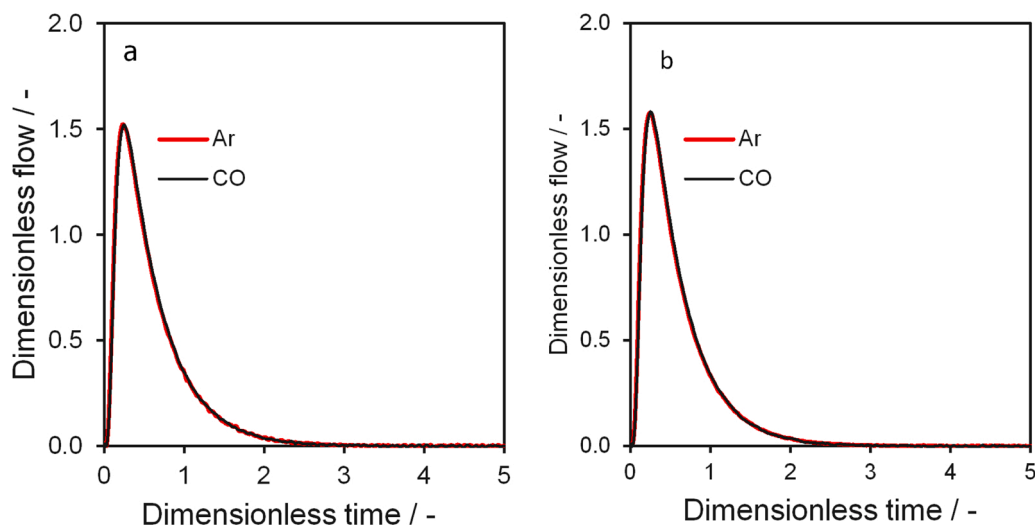


Fig. 9. Single-pulse responses of CO compared with the Ar response at 573 K over reduced (a) Au/TiO₂, and (b) Au/ZrO₂.

surface (yellow color), indicating the existence of strongly adsorbed carbon containing species (e.g., carbonate and formate species) and/or formation of a small amount of deposited carbon under the reaction condition.

3.3. Single-pulse TAP experiments

The interaction of CO₂ with the freshly reduced catalysts was investigated in the TAP reactor by injecting a single pulse of a CO₂/Ar mixture (CO₂: Ar = 1:1) in comparison to a pure Ar pulse over both catalysts at 300 °C. No gas-phase CO could be observed. This result unambiguously reveals that CO₂ cannot dissociate to CO under the conditions applied in this study. This result is also consistent with the in-situ DRIFT studies (vide infra, 3.4). Fig. 8 shows the dimensionless response of CO₂ and Ar obtained over both catalysts. The shape of CO₂ response of both catalysts shows broadening in comparison with the Ar response, which could be attributed to the desorption and re-adsorption of CO₂ and hence to a medium strong interaction of CO₂ with the catalyst [44]. A strong and broad CO₂ response curve is observed over the Au/TiO₂ catalyst (Fig. 8a) in contrast to a very weak response curve over the Au/ZrO₂ catalyst (Fig. 8b). The results show that CO₂ adsorption on Au/TiO₂ is weaker than on Au/ZrO₂. This strong adsorption is presumably the reason for the observed low RWGS activity over the

latter catalyst.

On the other hand, Fig. 9 also shows the dimensionless responses of CO and Ar obtained after pulsing a CO: Ar = 1:1 mixture over the freshly reduced catalysts. No obvious differences between these responses could be seen. This is a fingerprint for very weak adsorption of CO which might be the reason for the unprecedented CO selectivity observed over both catalysts even at high pressure of 20 bar (vide supra, Fig. S6).

3.4. In Situ DRIFTS studies

In-situ DRIFTS experiments were performed to monitor the evolution of carbon-containing species and to identify the possible intermediates during CO₂ hydrogenation over Au/TiO₂ and Au/ZrO₂. Before the spectral acquisition, the catalysts are reduced in H₂ at 300 °C for 2 h, then purged by He for 30 min at the same temperature to remove physisorbed species. The DRIFT spectra in the hydroxyl regions (Fig. S8) suggest the presence of surface hydroxyl groups on both catalysts after the reduction step. Fig. 10 shows the dynamic evolution of the carbon-containing species during CO₂ hydrogenation at 250 °C and 3 bar as a function of reaction time. Over Au/TiO₂, the spectrum exhibited a doublet at 2175 cm⁻¹ and 2108 cm⁻¹ due to the formation of gaseous CO in addition to several bands attributed to the formation bidentate formate and carbonate species. The bands at 1570 and 1359 cm⁻¹ were

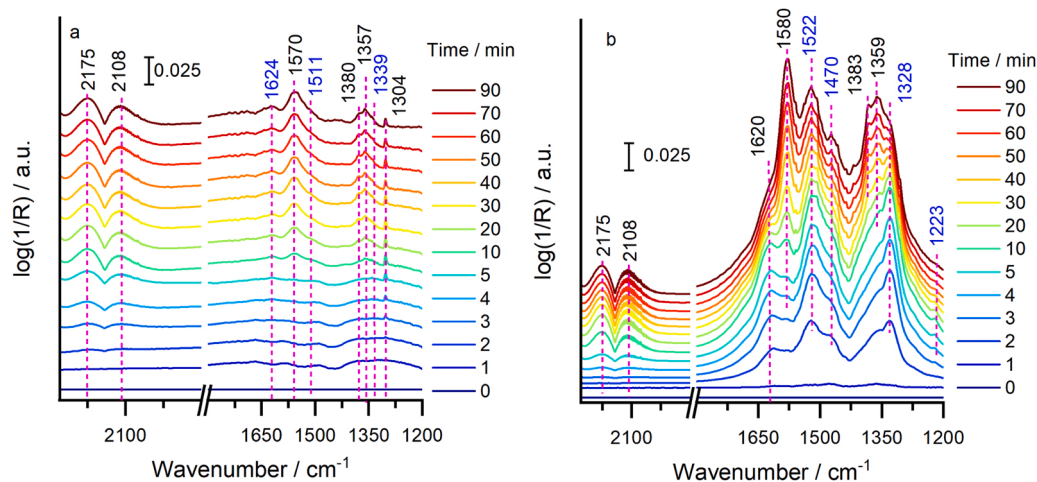


Fig. 10. In-situ DRIFT spectra of the RWGS reaction over (a) Au/TiO₂ (b) Au/ZrO₂ catalysts. Reaction conditions: P = 3 bar, H₂: CO₂: N₂ = 3:1:2; total flow rate = 18 ml/min, T = 250 °C.

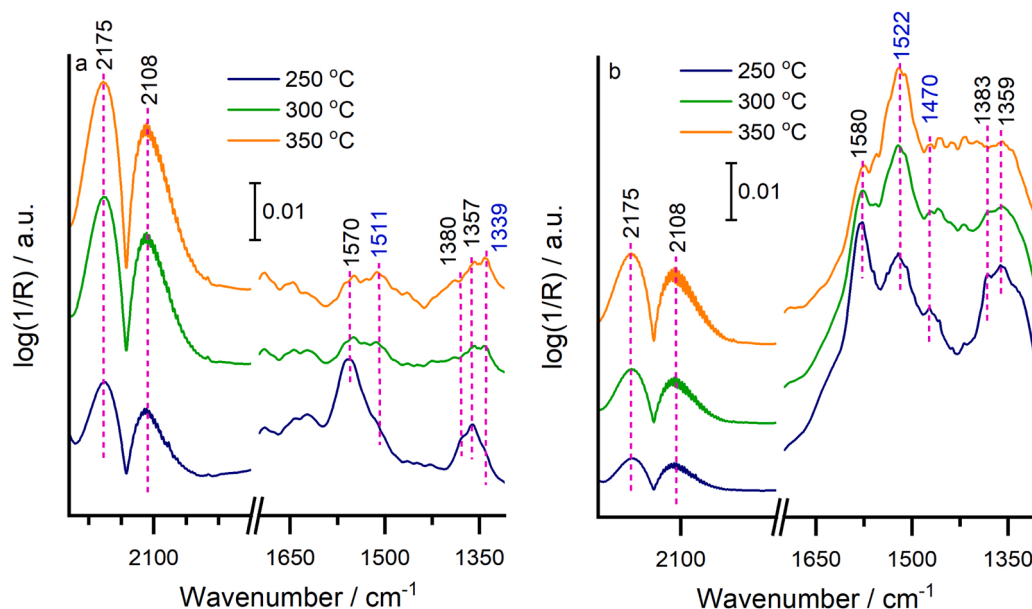


Fig. 11. In-situ DRIFT spectra of the RWGS reaction over (a) Au/TiO₂ (b) Au/ZrO₂ catalysts. Reaction conditions: P = 3 bar, H₂: CO₂: N₂ = 3:1:2; total flow rate = 18 ml/min.

assigned to the antisymmetric (ν_{as}) and symmetric (ν_s) OCO stretching vibrations of adsorbed bidentate formate (HCOO) species, respectively [45–49], while the band at 1380 cm⁻¹ was assigned to the CH bending ($\delta(\text{CH})$) vibration of the same species [45–49]. The bands at 1511 and 1339 cm⁻¹ can be assigned to the antisymmetric (ν_{as}) and symmetric (ν_s) OCO stretching vibrations of bidentate/unidentate carbonate (CO₃²⁻) species, respectively [45,48], while the band at 1620 cm⁻¹ could be attributed to the formation of bicarbonate or to a $\delta(\text{OH})$ -vibration of adsorbed water [50,51]. The carbonate and bicarbonate species are generally generated from the interaction between the CO₂ molecules with the coordinatively unsaturated O²⁻ of a metal oxide (cus-O²⁻) and the surface hydroxyl groups of support respectively [51,52].

For CO₂ hydrogenation over Au/ZrO₂ (Fig. 10b), the formation of formate (1580, 1380, and 1359 cm⁻¹) [46,53] and Monodentate carbonates (1522 and 1470 cm⁻¹) [45,49,51] are suggested. The spectra also suggest the formation of bicarbonate (HCO₃⁻) species (1622 ($\nu_{as}\text{OCO}$), 1328 ($\nu_s\text{OCO}$), and 1223 cm⁻¹ (δHOC)) [45,51,54]. The bicarbonates are formed by the interaction of CO₂ with the surface hydroxyl groups of ZrO₂ support [51,52]. At the beginning of the reaction, carbonate and bicarbonate are rapidly formed, and their intensities become apparent after 1 min. With prolonged reaction time, the bicarbonate-related bands (1622 and 1223 cm⁻¹) gradually began to decline, while the formate-related bands simultaneously grew and became more intense. This result suggests that the formate species are formed from the reduction of bicarbonate species, which is consistent with previous studies [13,55,56]. Because the activation of H₂ over ZrO₂ is negligible [51], the reduction of bicarbonate to formate species should occur by the activated hydrogen species spilled over from the gold species. In contrast to Au/ZrO₂ catalyst, the intensity of the carbonate and formates are barely visible until 10 min over Au/TiO₂. DRIFT experiments are also performed for the pure supports (TiO₂ and ZrO₂) (Fig. S9). The spectra over TiO₂ (Fig. S9a) suggest the formation of carbonate (1515 and 1339 cm⁻¹) and formate (1550, 1380, and 1359 cm⁻¹) species; however, they show an additional band at 1450 cm⁻¹ attributed to the symmetrically adsorbed carbonate species [57]. Similar to Au/ZrO₂, the spectra over ZrO₂ (Fig. S9b) show the evolution of bicarbonate (1328 cm⁻¹), carbonate (1470, 1557 cm⁻¹), and formate (1575 and 1375 cm⁻¹), but with much lower intensities. The significant improvement of CO₂ adsorption over Au/ZrO₂ compared with ZrO₂ is related to the generation of oxygen vacancies as proved by in-situ EPR (*Vide infra*, Fig. 13b),

suggesting the important role of oxygen vacancies in CO₂ adsorption and activation. It is also important to note that the adsorption of CO₂ is greatly enhanced over Au/ZrO₂ in comparison with Au/TiO₂. Sakurai et al. [11] attributed this behavior to the difference in the acid-base properties of the support. They showed that Au NPs supported on acidic oxides (e.g., TiO₂) gave higher CO₂ conversion than those supported on less acidic supports (e.g., ZrO₂) [11]. These differences in the CO₂ conversion were explained by the differences in the interaction of CO₂ with the support [11]. The relatively strong adsorption of CO₂ on less acidic supports like ZrO₂ results in a lower CO₂ hydrogenation activity [11].

Other DRIFTS experiments were also performed at 300 and 350 °C (Fig. 11), and the spectra were compared with those obtained at 250 °C. Over both catalysts, as the reaction temperature increases from 250° to 350°C, the signal intensity of bidentate formate species gradually decreases, while the signals related to bidentate/unidentate carbonates increase. These results indicate that the formate species are important intermediates during the RWGS reaction, while the carbonate species may act as spectators and more difficult to hydrogenate. It is also important to notice that, although Au/TiO₂ catalysts show much higher activity, the intensities of the formate species over Au/ZrO₂ remained much higher than those observed over Au/TiO₂. Hence, it seems obvious from DRIFTS that the formate mechanism might not be the main reaction mechanism over Au/TiO₂.

Several studies proposed that a redox mechanism exists on Pt/TiO₂ catalysts. They postulated that CO₂ adsorbs at the interface of Pt/TiO₂, in which the C atom adsorbs on Pt species, and one O adsorbs on an oxygen vacancy [58,59]. They suggested that the role of the oxygen vacancy is to trap the oxygen from CO₂ molecule and thus facilitate the cleavage of the C–O bond leading to the formation of CO [59]. Similarly, the formation of CO as a result of the dissociative adsorption of CO₂ has been reported on other supported noble metals (e.g., Rh/SiO₂ [60] or Au/CeO₂ catalysts [61]) and non-noble metals, especially the Cu based catalysts [8,62]. To investigate whether the redox mechanism can participate in our Au/TiO₂ or not. A further DRIFT experiment (not shown) was performed by flowing CO₂ without H₂ over pre-reduced Au/TiO₂. The DRIFT spectra indicate that, in the absence of hydrogen, CO₂ can only react with the surface of the TiO₂ support without any CO formation. This experiment demonstrates that the formation of CO from the dissociative adsorption of CO₂ over gold species or oxygen vacancies is not possible.

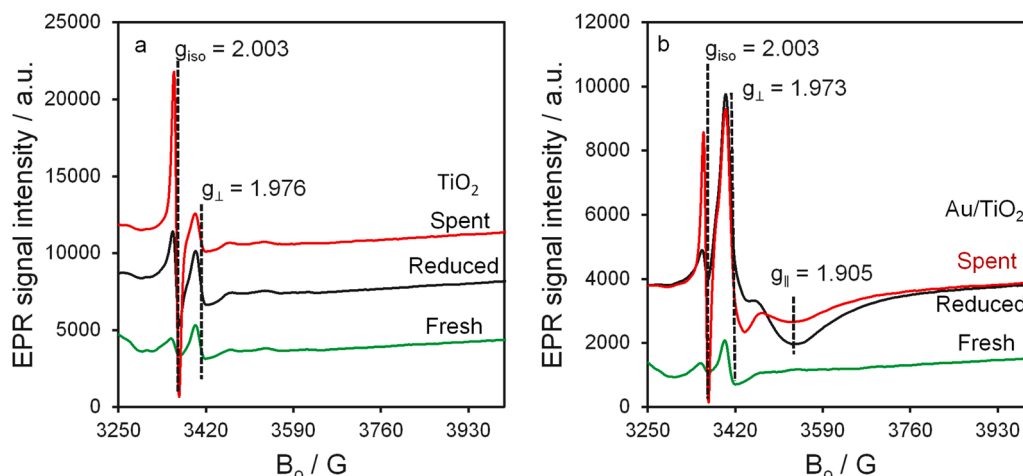


Fig. 12. In-situ EPR spectra obtained at 100 K for the as-obtained fresh, reduced (at 280 °C in 50% H₂/He for 2 h), and spent samples of (a) pure TiO₂ and (b) Au/TiO₂. Reaction conditions: P = 1 bar H₂; CO₂ = 3:1; total flow rate = 18 ml/min, T = 250 °C.

3.5. In-situ EPR studies

Oxygen vacancies are a common defect in reducible metal oxides. They can significantly affect their surface properties, enhance metal-support interactions, and, therefore, improve the thermal stability of the dispersed metal species. For instance, in TiO₂ and ZrO₂, the removal of oxygen anion is usually accompanied by the generation of oxygen vacancies and/or Ti³⁺ (Zr³⁺) centers. Ti³⁺ (3d¹) and Zr³⁺ (4d¹) species are formed by trapping of electrons from oxygen vacancies (e.g., O²⁻ + 2Ti⁴⁺ → O_v + 1/2O₂ + 2Ti³⁺). Accordingly, to uncover the role of supports on the reaction mechanisms, EPR measurements were performed for Au/TiO₂, Au/ZrO₂ catalysts, and the corresponding pure supports under near reaction conditions (at 1 bar) to confirm the presence of oxygen vacancies (O_v) and Ti³⁺ or Zr³⁺ sites. For the fresh TiO₂ support, the EPR spectrum (Fig. 12a) shows two EPR signals; an isotropic signal at g_{iso} = 2.0031 corresponding to the formation of oxygen vacancies with single trapped electrons [34,63] and another axial signal at g_⊥ = 1.976 and g_∥ = 1.926 attributed to the formation of Ti³⁺ sites [34,64,65]. After reduction with H₂, the signal intensity of oxygen vacancies and Ti³⁺ slightly increased. After feeding of the CO₂/H₂ mixture (spent form), the vacancy signal increased strongly. In contrast, no appreciable change in the EPR signals of Ti³⁺ was observed, suggesting that oxygen vacancies mostly trap the unpaired electrons. This effect was more pronounced after reaction (spent form) due to the exposure of the

catalyst to hydrogen-rich reaction conditions (75% H₂) for another 2 h.

Fig. 12b demonstrates a similar behavior for the oxygen vacancies signal in Au/TiO₂ catalyst, however, with much weaker intensity as shown in Fig. 12a, suggesting the electron transfer from oxygen vacancies to gold sites located at the interphase perimeter. These findings are consistent with the literature [66] and our XPS results (see XPS part), which prove the formation of electron-enriched Au species (Au^{δ-}). In contrast to the bare TiO₂, the axial signals of Ti³⁺ sites at g_⊥ = 1.9733 became much stronger, and their parallel components became broader and more shifted to g_∥ = 1.9051, suggesting that Au nanoparticles significantly boosted the generation of different Ti³⁺ species by H₂ activation and subsequent spillover onto the TiO₂ support. After the reaction, the intensity of the Ti³⁺ signal slightly decreased, this could be attributed to the partial transformation of Ti³⁺ to Ti⁴⁺ by re-filling the oxygen vacancies with CO₂.

For ZrO₂, Fig. 13a resolves two EPR signals on the fresh ZrO₂. The EPR signals at g_⊥ = 1.974 and g_∥ = 1.961 are assigned to Zr³⁺ species with axial symmetry [26,67], whereas the signal at g_{iso} = 2.002, similar to TiO₂, is due to a single electron trapped in an oxygen vacancy. Only a slight increase in the intensity of Zr³⁺ is observed when comparing the reduced and spent forms of the pure ZrO₂. As for Au/ZrO₂, the EPR spectrum of the fresh catalyst (Fig. 13b) shows the vacancy signal at g_{iso} = 2.003 and besides an axial signal at g_⊥ = 1.974 and g_∥ = 1.954 due to Zr³⁺ species. After reduction, the Zr³⁺ signal did not change while the

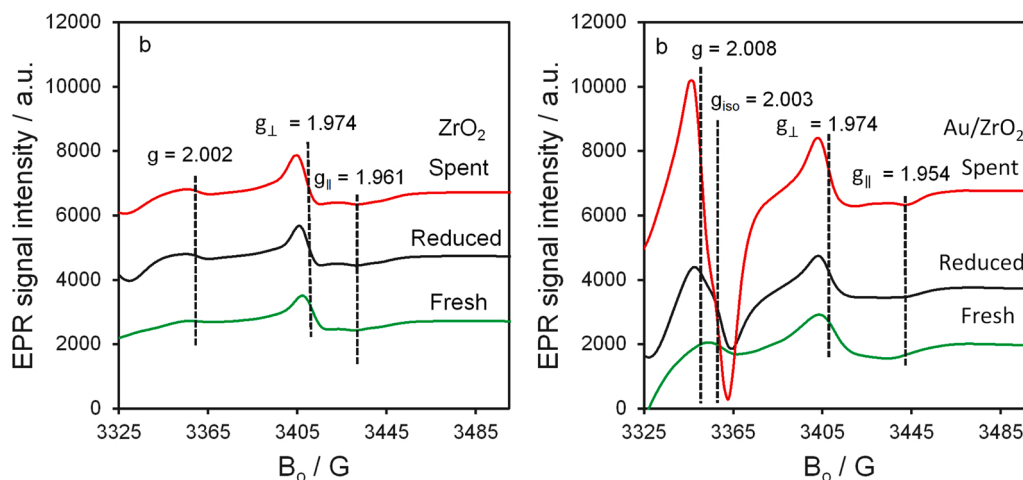
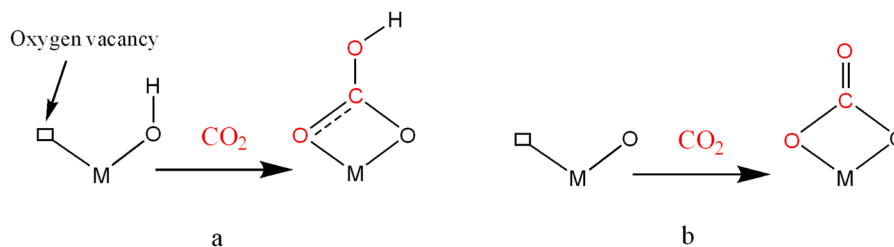


Fig. 13. In-situ EPR spectra obtained at 100 K for the as-obtained fresh, reduced (at 280 °C in 50% H₂/He for 2 h) and spent samples of (a) pure ZrO₂ and (b) Au/ZrO₂. Reaction conditions: P = 1 bar H₂; CO₂ = 3:1; total flow rate = 18 ml/min, T = 250 °C.



Scheme 1.

vacancy signal increased slightly. Similar to Au/TiO₂, this signal increased further in the spent catalyst. Additionally, it exhibited line broadening with a shoulder, suggesting a superposition of two EPR signals. For a better resolution of these, the second derivative of the EPR spectrum is presented in Fig. S10, which clearly shows the presence of an additional signal at a higher *g* value (2.008). This signal may be attributed to the formation of adsorbed bicarbonate/carbonate radicals [68]. The bicarbonate radicals (Scheme 1a) are most likely, formed by the interaction of CO₂ with the surface OH groups in the presence of oxygen vacancies, while the carbonate radicals (Scheme 1b) are formed by direct adsorption of CO₂ in the oxygen vacancies [69]. These results suggest that both the surface hydroxyl groups, and oxygen vacancies play a crucial role in the reaction mechanism of RWGS reaction over Au/ZrO₂.

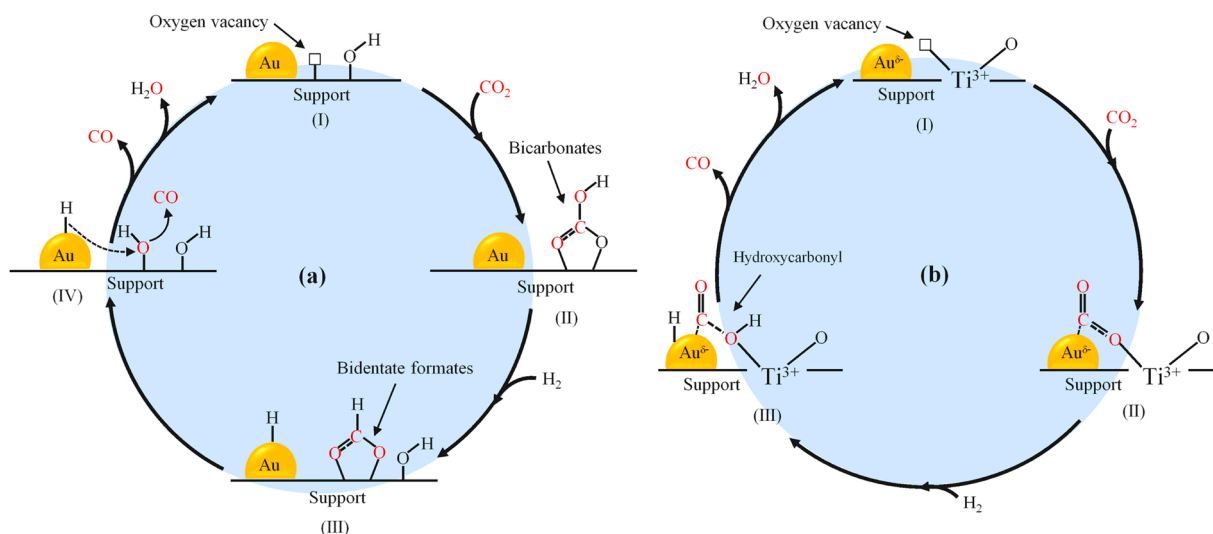
The strong increase in the vacancy signal after exposing the reduced catalyst to the CO₂/H₂ reaction mixture is surprising, since both atmospheres are reducing. A possible explanation is that a part of the formed O-vacancies after prereduction are EPR-silent, due to mutual magnetic interactions. These may become EPR-active upon transfer of their electrons to CO₂ molecules which form EPR-active bicarbonate/carbonate radicals (Scheme 1). This would “dilute” the paramagnetic vacancies and, thus reduce their mutual magnetic interactions. A similar conclusion was also drawn by Gionco et al. [26], who noticed that the majority of the formed oxygen vacancies on ZrO₂ are EPR silent and transformed to EPR active ones upon interaction with O₂ molecules. They attributed this spectral change to the electron transfer between the EPR-silent oxygen vacancies and the adsorbed O₂ molecules [26].

3.6. Reaction mechanism

Generally, two possible mechanisms, namely a redox and an associative mechanism, are suggested for the RWGS reaction [13]. In the

redox mechanism, H₂ dissociates on the surface into H atoms and reacts with surface O to form oxygen vacancies, which are subsequently filled by oxygen from CO₂ and produce CO. On the other hand, the associative mechanism suggests CO formation through the decomposition of the formate intermediate. In this work, considerable differences in the reaction mechanism on Au/TiO₂ and Au/ZrO₂ might be concluded. It is apparent from the in-situ DRIFT studies that the bicarbonate and the subsequently formed formate species are important intermediates for the RWGS reaction over Au/ZrO₂ catalyst. The spectra clearly indicate that surface hydroxyl groups are present on the zirconia surfaces, whereas the in-situ EPR studies suggest the formation of oxygen vacancies and adsorbed bicarbonate/carbonates radicals on Au/ZrO₂. Besides, the DRIFT experiments suggest that the carbonate species may act as spectators while the bicarbonates are the primary active intermediate. We propose that CO₂ molecules react first with the hydroxyl groups adjacent to oxygen vacancies producing bicarbonate species, which are then reduced to formate species by the activated hydrogen spilled over from the gold surface. The general steps of the proposed formate mechanism are depicted in Scheme 2a. The participation of carbonate species in the reaction mechanism cannot be excluded.

The formate pathway could also be in action over Au/TiO₂. However, the low concentration of the formate species, as observed in the DRIFT experiment (Fig. 10a), may suggest a higher decomposition rate of these species on Au/TiO₂ than on Au/ZrO₂. It is obvious from the TAP results that CO₂ is more strongly adsorbed on Au/ZrO₂ compared to the Au/TiO₂ catalyst. This strong adsorption on Au/ZrO₂ would directly lead to a significantly more stable reaction intermediate, i.e., more easily IR-detectable species. The formation of such stable intermediates on Au/ZrO₂ is presumably the reason for the observed low RWGS activity. In contrast, the weak adsorption of CO₂ on Au/TiO₂ led to the formation of less stable formate intermediates, i.e., much less IR-detectable species, which might rapidly decompose to CO. Hence, it is

Scheme 2. The proposed reaction mechanisms of the RWGS reaction over (a) Au/ZrO₂ and (b) Au/TiO₂ Catalysts.

reasonable to suggest that the formation and decomposition of formate intermediates could be the rate-determining step responsible for the difference in the activation energy values (vide supra, Fig. 6b).

Moreover, the higher decomposition rate of formate species over Au/TiO₂ could also attribute to the activation of hydrogen. It is noteworthy that the HAADF-STEM images (Fig. 3) reveal that small Au nanoparticles ($D_{Au} = 2-3$ nm) are predominantly formed over Au/TiO₂, while the gold species are distributed mainly as single sites over Au/ZrO₂ with very few Au NPs. Although the RWGS reactions over single site catalysts has been reported [70–72], there is some agreement in the literature that single-sites catalysts have higher H₂ activation barriers, and H₂ activation is greatly enhanced on supported metal NPs than on single-sites catalysts [16–18]. Based on this hypothesis, Au/TiO₂ is expected to have much higher concentration of activated H species than Au/ZrO₂. Accordingly, the high decomposition rate of the formate species over Au/TiO₂, and thus the higher catalytic activity, could be explained by enhanced H₂ activation over Au NPs.

Due to the low concentration of formate species on Au/TiO₂, the formate mechanism might not be the main reaction mechanism leading to CO formation. Rodríguez et al. [73] proposed the formation of hydroxycarbonyl (OCOH) as an active intermediate on Au/TiO₂ interface which, however, has a very short lifetime on the gold surface and hence cannot be detected by DRIFT [13,74]. Bobadilla et al. [13] also suggested the formation of hydroxycarbonyl (OCOH) species as key intermediates for RWGS [13]. They proposed that oxygen vacancies facilitate the formation of hydroxycarbonyl (OCOH) intermediates, which eventually decompose to form CO and H₂O [13].

In our study, the XPS results suggest the formation of electron-enriched Au species (Au^{δ-}) on the surface of TiO₂, which are supposed to play an important role in improving CO₂ adsorption and activation [10,75–77]. *In-situ* EPR measurements confirm the presence of Ti³⁺ species and oxygen vacancies (Fig. 12b). Moreover, EELS results (Fig. 3) reveal that Ti³⁺ are predominantly formed in the shell region of TiO₂ particles. These results suggest that O_v-Ti³⁺ sites participate in the reaction mechanism and serve as an active site for RWGS. Accordingly, we anticipate that on Au/TiO₂ the RWGS reaction follows the hydroxycarbonyl pathway (Scheme 2b). We suggest that Au-O_v-Ti³⁺ moieties are the active sites responsible for CO₂ activation and conversion to CO. We propose that CO₂ molecules are first activated on Au-O_v-Ti³⁺ sites. The activated CO₂ molecules are then hydrogenated to hydroxycarbonyl (OCOH) species. Due to the relatively short lifetime of these species, they rapidly decompose to weakly adsorbed CO on the Au surface and OH. Eventually, the adsorbed H and the formed OH species react to H₂O and regenerate the oxygen vacancies. The formation of a shell of Ti³⁺ around TiO₂ (evidenced by EELS, Fig. 3) may facilitate the removal of formed OH on Ti³⁺ since it has been shown to play a role in destabilizing surface species. (e.g., OH) [78].

It is noteworthy that we cannot rule out the involvement of the redox system (O_v-Ti³⁺ ↔ O-Ti⁴⁺) in the reaction mechanism during CO₂ reduction, which frequently discussed in literature. However, we did not find any experimental evidence in support of the formation of CO₂[•] radical and CO₂ species. As CO₂[•] radical and CO₂ species are expected to form by reducing CO₂ molecules by one and two electron transfers, respectively, from oxygen vacancies and/or Ti³⁺. The prominent role of the gold species is to activate the hydrogen and increase the density of oxygen vacancies and, therefore, the number of Au-O_v-Ti³⁺ sites available for CO₂ activation. It is noteworthy that the participation of the associative (formate) mechanism cannot be excluded. The detected formate species (Fig. 10a) may represent a minor contribution of the associative mechanism to the overall catalytic reaction. In summary, our results show that both the surface defects (oxygen vacancies) and the gold NPs play critical roles in the activation of CO₂ and H₂.

4. Conclusions

Hydrogenation of CO₂ has been studied over Au/TiO₂ and Au/ZrO₂ catalysts with very low gold loadings of < 0.1% at different reaction conditions. Superior activity and 100% CO selectivity were achieved with Au/TiO₂ that showed a 10 time higher CO formation rate than Au/ZrO₂ at 250 °C. Gold species with a partial negative charge (Au^{δ-}) are present as nanoparticles and single sites on TiO₂ and ZrO₂, respectively. However, the chemical state of the Au/TiO₂ catalyst revealed significant differences compared to Au/ZrO₂. In the former, transformation of Ti⁴⁺ to Ti³⁺ was observed in the interface region, suggesting the formation of Au^{δ-}-O_v-Ti³⁺ sites that serve as active sites for RWGS reaction and are responsible for the superior performance of Au/TiO₂.

Different reaction mechanisms were found for the two catalysts. On Au/ZrO₂, RWGS proceeds via the formate mechanism, in which CO₂ adsorbs strongly in oxygen vacancies and is activated via formation of a formate species that releases CO. This strong adsorption of CO₂ might be the reason for the low activity of Au/ZrO₂. In contrast, CO is formed mainly through hydroxycarbonyl intermediate species on Au/TiO₂, though a minor contribution of the formate mechanism cannot be excluded. In summary, we have clearly shown that surface defects (oxygen vacancies), combined with facile decomposition of the formed intermediates are essential for high RWGS rates.

CRedit authorship contribution statement

Abdallah. I. M. Rabee: Conceptualization, Investigation, Writing – original draft. **Dan Zhao:** Investigation. **Sebastian Cisneros:** Investigation. **Carsten R. Kreyenschulte:** Investigation. **Vita Kondratenko:** Investigation. **Stephan Bartling:** Investigation. **Christoph Kubis:** Investigation. **Evgenii V. Kondratenko:** Investigation and validation. **Angelika Brückner:** Conceptualization, Supervision. **Jabor Rabeah:** Conceptualization, Investigation, Supervision, Writing – review & editing.

Declaration of Competing Interest

The authors declare the following financial interests/personal relationships which may be considered as potential competing interests: Abdallah. I. M. Rabee reports financial support was provided by The Alexander von Humboldt Foundation. Carsten R. Kreyenschulte reports equipment, drugs, or supplies was provided by the Federal German Ministry for Education and Science (BMBF). Jabor Rabeah reports financial support was provided by The European Commission H2020.

Data availability

Data will be made available on request.

Acknowledgments

A.I.M.R. gratefully appreciates the Alexander von Humboldt Foundation (Bonn, Germany) for a postdoctoral fellowship program, and Minia University administration/Egypt for a leave of absence. The authors acknowledge the Federal German Ministry for Education and Science (BMBF) for funding the electron energy loss spectrometer within the project ESMAC. Financial support from the European Commission through the H2020-MSCA-RISE-2020 BIOALL project (Grant Agreement: 101008058) is also acknowledged.

Appendix A. Supporting information

Supplementary data associated with this article can be found in the online version at [doi:10.1016/j.apcatb.2022.122083](https://doi.org/10.1016/j.apcatb.2022.122083).

References

- [1] W. Wang, S. Wang, X. Ma, J. Gong, Recent advances in catalytic hydrogenation of carbon dioxide, *Chem. Soc. Rev.* 40 (2011) 3703–3727.
- [2] J. Li, Y. He, L. Tan, P. Zhang, X. Peng, A. Oruganti, G. Yang, H. Abe, Y. Wang, N. Tsubaki, Integrated tuneable synthesis of liquid fuels via Fischer–Tropsch technology, *Nat. Catal.* 1 (2018) 787–793.
- [3] Y.A. Daza, J.N. Kuhn, CO₂ conversion by reverse water gas shift catalysis: comparison of catalysts, mechanisms and their consequences for CO₂ conversion to liquid fuels, *RSC Adv.* 6 (2016) 49675–49691.
- [4] M. Ronda-Lloret, S. Rico-Francés, A. Sepúlveda-Escribano, E.V. Ramos-Fernandez, CuOx/CeO₂ catalyst derived from metal organic framework for reverse water-gas shift reaction, *Appl. Catal. A: Gen.* 562 (2018) 28–36.
- [5] C.-S. Chen, W.-H. Cheng, S.-S. Lin, Study of iron-promoted Cu/SiO₂ catalyst on high temperature reverse water gas shift reaction, *Appl. Catal. A: Gen.* 257 (2004) 97–106.
- [6] R. Jin, J. Easa, C.P. O'Brien, Highly Active Cu₂O/SiO₂ Dot Core/Rod Shell Catalysts with Enhanced Stability for the Reverse Water Gas Shift Reaction, *ACS Appl. Mater. Interfaces* 13 (2021) 38213–38220.
- [7] X. Su, X. Yang, B. Zhao, Y. Huang, Designing of highly selective and high-temperature durable RWGS heterogeneous catalysts: recent advances and the future directions, *J. Energy Chem.* 26 (2017) 854–867.
- [8] X. Zhang, X. Zhu, L. Lin, S. Yao, M. Zhang, X. Liu, X. Wang, Y.-W. Li, C. Shi, D. Ma, Highly Dispersed Copper over β -Mo₂C as an Efficient and Stable Catalyst for the Reverse Water Gas Shift (RWGS) Reaction, *ACS Catal.* 7 (2017) 912–918.
- [9] N. Ishito, K. Hara, K. Nakajima, A. Fukuoka, Selective synthesis of carbon monoxide via formates in reverse water–gas shift reaction over alumina-supported gold catalyst, *J. Energy Chem.* 25 (2016) 306–310.
- [10] C. Wu, P. Zhang, Z. Zhang, L. Zhang, G. Yang, B. Han, Efficient Hydrogenation of CO₂ to Methanol over Supported Subnanometer Gold Catalysts at Low Temperature, *ChemCatChem* 9 (2017) 3691–3696.
- [11] H. Sakurai, S. Tsubota, M. Haruta, Hydrogenation of CO₂ over gold supported on metal oxides, *Appl. Catal. A: Gen.* 102 (1993) 125–136.
- [12] X. Zhu, X. Qu, X. Li, J. Liu, J. Liu, B. Zhu, C. Shi, Selective reduction of carbon dioxide to carbon monoxide over Au/CeO₂ catalyst and identification of reaction intermediate, *Chinese J. Catal.* 37 (2016) 2053–2058.
- [13] L.F. Bobadilla, J.L. Santos, S. Ivanova, J.A. Odriozola, A. Urakawa, Unravelling the Role of Oxygen Vacancies in the Mechanism of the Reverse Water–Gas Shift Reaction by Operando DRIFTS and Ultraviolet–Visible Spectroscopy, *ACS Catal.* 8 (2018) 7455–7467.
- [14] B. Hu, Y. Yin, G. Liu, S. Chen, X. Hong, S.C.E. Tsang, Hydrogen spillover enabled active Cu sites for methanol synthesis from CO₂ hydrogenation over Pd doped CuZn catalysts, *J. Catal.* 359 (2018) 17–26.
- [15] D. Xu, X. Hong, G. Liu, Highly dispersed metal doping to ZnZr oxide catalyst for CO₂ hydrogenation to methanol: Insight into hydrogen spillover, *J. Catal.* 393 (2021) 207–214.
- [16] R. Gao, J. Xu, J. Wang, J. Lim, C. Peng, L. Pan, X. Zhang, H. Yang, J.-J. Zou, Pd/Fe₂O₃ with Electronic Coupling Single-Site Pd–Fe Pair Sites for Low-Temperature Semihydrogenation of Alkynes, *J. Am. Chem. Soc.* 144 (2022) 573–581.
- [17] M. Zhou, M. Yang, X. Yang, X. Zhao, L. Sun, W. Deng, A. Wang, J. Li, T. Zhang, On the mechanism of H₂ activation over single-atom catalyst: An understanding of Pt₁/WO₃ in the hydrogenolysis reaction, *Chinese J. Catal.* 41 (2020) 524–532.
- [18] H.-Y.T. Chen, S. Tosoni, G. Pacchioni, Hydrogen Adsorption, Dissociation, and Spillover on Ru₁₀ Clusters Supported on Anatase TiO₂ and Tetragonal ZrO₂ (101) Surfaces, *ACS Catal.* 5 (2015) 5486–5495.
- [19] M. Sankar, Q. He, R.V. Engel, M.A. Sainna, A.J. Logsdail, A. Roldan, D.J. Willock, N. Agarwal, C.J. Kiely, G.J. Hutchings, Role of the Support in Gold-Containing Nanoparticles as Heterogeneous Catalysts, *Chem. Rev.* 120 (2020) 3890–3938.
- [20] D. Pakhare, J. Spivey, A review of dry (CO₂) reforming of methane over noble metal catalysts, *Chem. Soc. Rev.* 43 (2014) 7813–7837.
- [21] V. Kyriakou, A. Vourros, I. Garagounis, S.A.C. Carabineiro, F.J. Maldonado-Hódar, G.E. Marnellos, M. Konsolakis, Highly active and stable TiO₂-supported Au nanoparticles for CO₂ reduction, *Catal. Commun.* 98 (2017) 52–56.
- [22] T. Montini, M. Melchionna, M. Monai, P. Fornasiero, Fundamentals and Catalytic Applications of CeO₂-Based Materials, *Chem. Rev.* 116 (2016) 5987–6041.
- [23] D. Wang, Q. Bi, G. Yin, W. Zhao, F. Huang, X. Xie, M. Jiang, Direct synthesis of ethanol via CO₂ hydrogenation using supported gold catalysts, *Chem. Commun.* 52 (2016) 14226–14229.
- [24] G.K. Ramesha, J.F. Brennecke, P.V. Kamat, Origin of Catalytic Effect in the Reduction of CO₂ at Nanostructured TiO₂ Films, *ACS Catal.* 4 (2014) 3249–3254.
- [25] K. Li, J.G. Chen, CO₂ Hydrogenation to Methanol over ZrO₂-Containing Catalysts: Insights into ZrO₂ Induced Synergy, *ACS Catal.* 9 (2019) 7840–7861.
- [26] C. Gionco, M.C. Paganini, E. Giamello, R. Burgess, C. Di Valentin, G. Pacchioni, Paramagnetic Defects in Polycrystalline Zirconia: An EPR and DFT Study, *Chem. Mater.* 25 (2013) 2243–2253.
- [27] H. Chen, Z. Zhao, G. Wang, Z. Zheng, J. Chen, Q. Kuang, Z. Xie, Dynamic Phase Transition of Iron Oxy-carbide Facilitated by Pt Nanoparticles for Promoting the Reverse Water Gas Shift Reaction, *ACS Catal.* 11 (2021) 14586–14595.
- [28] J.H. Scofield, Hartree-Slater subshell photoionization cross-sections at 1254 and 1487 eV, *J. Electron. Spectrosc. Relat. Phenom.* 8 (1976) 129–137.
- [29] K. Morgan, N. Maguire, R. Fushimi, J.T. Gleaves, A. Goguet, M.P. Harold, E. V. Kondratenko, U. Menon, Y. Schuurman, G.S. Yablonsky, Forty years of temporal analysis of products, *Catal. Sci. Technol.* 7 (2017) 2416–2439.
- [30] J.T. Gleaves, G.S. Yablonsky, P. Phanawadee, Y. Schuurman, TAP-2: An interrogative kinetics approach, *Appl. Catal. A: Gen.* 160 (1997) 55–88.
- [31] J. Pérez-Ramírez, E.V. Kondratenko, Evolution, achievements, and perspectives of the TAP technique, *Catal. Today* 121 (2007) 160–169.
- [32] M. Rothaemel, M. Baerns, Modeling and Simulation of Transient Adsorption and Reaction in Vacuum Using the Temporal Analysis of Products Reactor, *Ind. Eng. Chem. Res.* 35 (1996) 1556–1565.
- [33] M. Soick, D. Wolf, M. Baerns, Determination of kinetic parameters for complex heterogeneous catalytic reactions by numerical evaluation of TAP experiments, *Chem. Eng. Sci.* 55 (2000) 2875–2882.
- [34] S. Cisneros, A. Abdel-Mageed, J. Mosrati, S. Bartling, N. Rockstroh, H. Atia, H. Abed, J. Rabeah, A. Brückner, Oxygen vacancies in Ru/TiO₂ - drivers of low-temperature CO₂ methanation assessed by multimodal operando spectroscopy, *iScience* 25 (2022), 103886.
- [35] A.I.M. Rabee, S.D. Le, K. Higashimura, S. Nishimura, Aerobic oxidation of 5-hydroxymethylfurfural into 2,5-furandicarboxylic acid over gold stabilized on zirconia-based supports, *ACS Sustain. Chem. Eng.* 8 (2020) 7150–7161.
- [36] K.S.W. Sing, The use of gas adsorption for the characterization of porous solids, *Colloids Surf.* 38 (1989) 113–124.
- [37] M. Thommes, K. Kaneko, A.V. Neimark, J.P. Olivier, F. Rodriguez-Reinoso, J. Rouquerol, K.S.W. Sing, Physisorption of gases, with special reference to the evaluation of surface area and pore size distribution (IUPAC Technical Report), *Pure Appl. Chem.* 87 (2015) 1051–1069.
- [38] A. Gloter, C. Ewels, P. Umek, D. Arcon, C. Colliex, Electronic structure of titania-based nanotubes investigated by EELS spectroscopy, *Phys. Rev. B* 80 (2009), 035413.
- [39] T. Arita, M. Kohyama, Visualization of the distribution of anatase and rutile TiO₂ crystals in Au/TiO₂ powder catalysts by STEM–EELS spectrum imaging, *Surf. Interface Anal.* 46 (2014) 1249–1252.
- [40] J. Radnik, K. Mohr, P. Claus, On the origin of binding energy shifts of core levels of supported gold nanoparticles and dependence of pretreatment and material synthesis, *Phys. Chem. Chem. Phys.* 5 (2003) 172–177.
- [41] G. Jacobs, P.M. Patterson, L. Williams, E. Chenu, D. Sparks, G. Thomas, B.H. Davis, Water-gas shift: in situ spectroscopic studies of noble metal promoted ceria catalysts for CO removal in fuel cell reformers and mechanistic implications, *Appl. Catal. A: Gen.* 262 (2004) 177–187.
- [42] M. Gonzalez Castaño, T.R. Reina, S. Ivanova, M.A. Centeno, J.A. Odriozola, Pt vs. Au in water–gas shift reaction, *J. Catal.* 314 (2014) 1–9.
- [43] N.H.M.D. Dostagir, R. Rattanawan, M. Gao, J. Ota, J.-Y. Hasegawa, K. Asakura, A. Fukouka, A. Shrotri, Co Single Atoms in ZrO₂ with Inherent Oxygen Vacancies for Selective Hydrogenation of CO₂ to CO, *ACS Catal.* 11 (2021) 9450–9461.
- [44] M. Kotobuki, R. Leppelt, D.A. Hansgen, D. Widmann, R.J. Behm, Reactive oxygen on a Au/TiO₂ supported catalyst, *J. Catal.* 264 (2009) 67–76.
- [45] D. Bianchi, T. Chafik, M. Khalfallah, S.J. Teichner, Intermediate species on zirconia supported methanol aerogel catalysts: II. Adsorption of carbon monoxide on pure zirconia and on zirconia containing zinc oxide, *Appl. Catal. A: Gen.* 105 (1993) 223–249.
- [46] J. Araña, C. Garriga, i Cabo, J.M. Doña-Rodríguez, O. González-Díaz, J.A. Herrera-Melián, J. Pérez-Peña, FTIR study of formic acid interaction with TiO₂ and TiO₂ doped with Pd and Cu in photocatalytic processes, *Appl. Surf. Sci.* 239 (2004) 60–71.
- [47] K. Larmier, W.-C. Liao, S. Tada, E. Lam, R. Verel, A. Bansode, A. Urakawa, A. Comas-Vives, C. Copéret, CO₂-to-Methanol Hydrogenation on Zirconia-Supported Copper Nanoparticles: Reaction Intermediates and the Role of the Metal-Support, *Interface, Angew. Chem. Int. Ed.* 56 (2017) 2318–2323.
- [48] S. Eckle, Y. Denkwitz, R.J. Behm, Activity, selectivity, and adsorbed reaction intermediates/reaction side products in the selective methanation of CO in reformate gases on supported Ru catalysts, *J. Catal.* 269 (2010) 255–268.
- [49] B. Yan, B. Zhao, S. Kattel, Q. Wu, S. Yao, D. Su, J.G. Chen, Tuning CO₂ hydrogenation selectivity via metal-oxide interfacial sites, *J. Catal.* 374 (2019) 60–71.
- [50] J.-D. Grunwaldt, M. Maciejewski, O.S. Becker, P. Fabrizioli, A. Baiker, Comparative Study of Au/TiO₂ and Au/ZrO₂ Catalysts for Low-Temperature CO Oxidation, *J. Catal.* 186 (1999) 458–469.
- [51] I.A. Fisher, A.T. Bell, In-Situ Infrared Study of Methanol Synthesis from H₂/CO₂ over Cu/SiO₂ and Cu/ZrO₂/SiO₂, *J. Catal.* 172 (1997) 222–237.
- [52] T. Horiuchi, H. Hidaka, T. Fukui, Y. Kubo, M. Horio, K. Suzuki, T. Mori, Effect of added basic metal oxides on CO₂ adsorption on alumina at elevated temperatures, *Appl. Catal. A: Gen.* 167 (1998) 195–202.
- [53] M.-Y. He, J.M. White, J.G. Ekerdt, CO and CO₂ hydrogenation over metal oxides: a comparison of ZnO, TiO₂ and ZrO₂, *J. Mol. Catal.* 30 (1985) 415–430.
- [54] K. Pokrovski, K.T. Jung, A.T. Bell, Investigation of CO and CO₂ Adsorption on Tetragonal and Monoclinic Zirconia, *Langmuir* 17 (2001) 4297–4303.
- [55] X. Wang, H. Shi, J.H. Kwak, J. Szanyi, Mechanism of CO₂ Hydrogenation on Pd/Al₂O₃ Catalysts: Kinetics and Transient DRIFTS-MS Studies, *ACS Catal.* 5 (2015) 6337–6349.
- [56] X. Wang, Y. Hong, H. Shi, J. Szanyi, Kinetic modeling and transient DRIFTS-MS studies of CO₂ methanation over Ru/Al₂O₃ catalysts, *J. Catal.* 343 (2016) 185–195.
- [57] K.K. Bando, K. Sayama, H. Kusama, K. Okabe, H. Arakawa, In-situ FT-IR study on CO₂ hydrogenation over Cu catalysts supported on SiO₂, Al₂O₃, and TiO₂, *Appl. Catal. A: Gen.* 165 (1997) 391–409.
- [58] S.S. Kim, H.H. Lee, S.C. Hong, A study on the effect of support's reducibility on the reverse water-gas shift reaction over Pt catalysts, *Appl. Catal. A: Gen.* 423–424 (2012) 100–107.
- [59] S. Kattel, B. Yan, J.G. Chen, P. Liu, CO₂ hydrogenation on Pt, Pt/SiO₂ and Pt/TiO₂: Importance of synergy between Pt and oxide support, *J. Catal.* 343 (2016) 115–126.

- [60] I.A. Fisher, A.T. Bell, A Comparative Study of CO and CO₂ Hydrogenation over Rh/SiO₂, *J. Catal.* 162 (1996) 54–65.
- [61] L.C. Wang, M. Tahvildar Khazaneh, D. Widmann, R.J. Behm, TAP reactor studies of the oxidizing capability of CO₂ on a Au/CeO₂ catalyst – A first step toward identifying a redox mechanism in the Reverse Water–Gas Shift reaction, *J. Catal.* 302 (2013) 20–30.
- [62] J. Nakamura, J.A. Rodriguez, C.T. Campbell, Does CO₂ dissociatively adsorb on Cu surfaces? *J. Phys.: Condens. Matter* 1 (1989) SB149–SB160.
- [63] J.M. Coronado, A.J. Maira, J.C. Conesa, K.L. Yeung, V. Augugliaro, J. Soria, EPR Study of the Surface Characteristics of Nanostructured TiO₂ under UV Irradiation, *Langmuir* 17 (2001) 5368–5374.
- [64] M. Chiesa, M.C. Paganini, S. Livraghi, E. Giamello, Charge trapping in TiO₂ polymorphs as seen by Electron Paramagnetic Resonance spectroscopy, *Phys. Chem. Chem. Phys.* 15 (2013) 9435–9447.
- [65] S. Livraghi, M. Chiesa, M.C. Paganini, E. Giamello, On the Nature of Reduced States in Titanium Dioxide As Monitored by Electron Paramagnetic Resonance. I: The Anatase Case, *J. Phys. Chem. C* 115 (2011) 25413–25421.
- [66] J.B. Priebe, J. Radnik, C. Kreyenschulte, A.J.J. Lennox, H. Junge, M. Beller, A. Brückner, H₂ Generation with (Mixed) Plasmonic Cu/Au-TiO₂ Photocatalysts: Structure–Reactivity Relationships Assessed by in situ Spectroscopy, *ChemCatChem* 9 (2017) 1025–1031.
- [67] S. Chen, A.M. Abdel-Mageed, M. Li, S. Cisneros, J. Bansmann, J. Rabeeah, A. Brückner, A. Groß, R.J. Behm, Electronic metal-support interactions and their promotional effect on CO₂ methanation on Ru/ZrO₂ catalysts, *J. Catal.* 400 (2021) 407–420.
- [68] F. Callens, G. Vanhaelewyn, P. Matthys, E. Boesman, EPR of carbonate derived radicals: Applications in dosimetry, dating and detection of irradiated food, *Appl. Magn. Reson.* 14 (1998) 235–254.
- [69] B. Liu, C. Li, G. Zhang, X. Yao, S.S.C. Chuang, Z. Li, Oxygen Vacancy Promoting Dimethyl Carbonate Synthesis from CO₂ and Methanol over Zr-Doped CeO₂ Nanorods, *ACS Catal.* 8 (2018) 10446–10456.
- [70] L. Chen, R.R. Unocic, A.S. Hoffman, J. Hong, A.H. Braga, Z. Bao, S.R. Bare, J. Szanyi, Unlocking the Catalytic Potential of TiO₂-Supported Pt Single Atoms for the Reverse Water–Gas Shift Reaction by Altering Their Chemical Environment, *JACS Au* 1 (2021) 977–986.
- [71] M.-M. Millet, G. Algara-Siller, S. Wrabetz, A. Mazheika, F. Girgsdies, D. Teschner, F. Seitz, A. Tarasov, S.V. Levchenko, R. Schlögl, E. Frei, Ni Single Atom Catalysts for CO₂ Activation, *J. Am. Chem. Soc.* 141 (2019) 2451–2461.
- [72] Y. Tang, C. Asokan, M. Xu, G.W. Graham, X. Pan, P. Christopher, J. Li, P. Sautet, Rh single atoms on TiO₂ dynamically respond to reaction conditions by adapting their site, *Nat. Commun.* 10 (2019) 4488.
- [73] J.A. Rodríguez, J. Evans, J. Graciani, J.-B. Park, P. Liu, J. Hrbek, J.F. Sanz, High Water–Gas Shift Activity in TiO₂ (110) Supported Cu and Au Nanoparticles: Role of the Oxide and Metal Particle Size, *J. Phys. Chem. C* 113 (2009) 7364–7370.
- [74] S.D. Senanayake, D. Stacchiola, P. Liu, C.B. Mullins, J. Hrbek, J.A. Rodríguez, Interaction of CO with OH on Au(111): HCOO, CO₃, and HOCO as Key Intermediates in the Water-Gas Shift Reaction, *J. Phys. Chem. C* 113 (2009) 19536–19544.
- [75] M.-C. Silaghi, A. Comas-Vives, C. Copéret, CO₂ Activation on Ni/γ-Al₂O₃ Catalysts by First-Principles Calculations: From Ideal Surfaces to Supported Nanoparticles, *ACS Catal.* 6 (2016) 4501–4505.
- [76] J. Li, X. Zhao, Z. Ma, Y. Pei, Structure and catalytic activity of gold clusters supported on nitrogen-doped graphene, *J. Phys. Chem. C* 125 (2021) 5006–5019.
- [77] L.-Y. Lin, S. Kavadiya, X. He, W.-N. Wang, B.B. Karakocak, Y.-C. Lin, M.Y. Berezin, P. Biswas, Engineering stable Pt nanoparticles and oxygen vacancies on defective TiO₂ via introducing strong electronic metal-support interaction for efficient CO₂ photoreduction, *Chem. Eng. J.* 389 (2020), 123450.
- [78] S. Huygh, A. Bogaerts, E.C. Neyts, How Oxygen Vacancies Activate CO₂ Dissociation on TiO₂ Anatase (001), *J. Phys. Chem. C* 120 (2016) 21659–21669.